Visualizing the Electron Wind Force in the Elastic Regime

Matthew Mecklenburg,[1,2*] Brian T. Zutter,[3,4] Xin Yi Ling[3],
William A. Hubbard,[3,4] B. C. Regan[3,4]

[1]Core Center of Excellence in Nano Imaging (CNI), University of Southern California,
Los Angeles, CA, 90089, U.S.A
[2]Microelectronics Technology Department, The Aerospace Corporation,
Los Angeles, CA, 90009, U.S.A
[3]Department of Physics and Astronomy, University of California,
Los Angeles, CA 90095, U.S.A
[4]California NanoSystems Institute, University of California,
Los Angeles, CA 90095, U.S.A

With continued scaling toward higher component densities, integrated circuits (ICs) contain ever greater lengths of nanowire vulnerable to failure via electromigration. Previously, plastic electromigration driven by the 'electron wind' has been observed, but not the elastic response to the wind force itself. Here we describe mapping, via electron energy-loss spectroscopy, the density of a lithographically-defined aluminum nanowire with sufficient precision to determine both its temperature and its internal pressure. An electrical current density of 10^8 A/cm^2 produces Joule heating, tension upwind, and compression downwind. Surprisingly, the pressure returns to its ambient value well inside the wire, where the current density is still high. This spatial discrepancy points to physics not captured by a classical 'wind force' model, and to new opportunities for optimizing electromigration-resistant IC design.

Keywords: *electromigration, electron wind force, plasmons, pressure, EELS, in situ TEM*

Electromigration is the most important threat to the reliability of interconnects in integrated circuits (ICs)[1–3]. As continued scaling leads to smaller metallization volumes, interconnect resistances are increasing exponentially[4]. Larger current densities and narrower wires make failures due to electromigration more likely. Simultaneously, because of the increasing total length of interconnect, robustness to electromigration must increase simply to maintain current levels of IC reliability. The resulting squeeze creates a technological horizon only a few years out, beyond which manufacturable solutions are not known[2,5].

To minimize the electromigration constraints on circuit performance, IC designers consider all aspects of interconnect geometry and nanostructure, from the wire material to its routing, cladding, capping, curvature, and grain structure[5,6]. Importantly, they increasingly rely on the short–length (or Blech) effect[7,8], namely that, at a given current density and temperature, electromigration is self-limiting in wires shorter than the threshold 'Blech length'. This short-length effect arises because the atomic motion produced by electromigration leads to a back-stress gradient (i.e. an opposing stress migration) such that the net migration eventually comes to a halt[2]. No measurements of back stress in wires less than 10 μm long have been reported[7,9–21]. Furthermore, the 'transient' electromigration forces observed previously build up over time as the result of atomic diffusion and thus represent plastic deformations[10,12,17,20]. No previous study has observed the electron wind force that directs the atomic diffusion and is thus the ultimate source of electromigration. The wind force produces an elastic, Hooke's-law response created by atoms displaced from their equilibrium positions but not moving between lattice sites[19]. Because the wind force is proportional to the electric current density J, both it and the induced elastic response vanish immediately when the electric current is interrupted.

Here we present an imaging technique with nanometer-scale spatial resolution and sufficient sensitivity to detect the electron wind force in the elastic regime. Based on electron energy loss

spectroscopy (EELS) in a scanning transmission electron microscope (STEM), the measurement technique maps the bulk plasmon energy E_p in a current-carrying wire. In an electron gas model the plasmon energy,

$$E_p = \hbar\sqrt{\frac{e^2 n}{\epsilon_0 m}}, \tag{1}$$

depends only on the valence electron density n and fundamental constants: the electron mass m, the elementary charge $e > 0$, the reduced Planck's constant $\hbar$, and the vacuum permittivity ϵ_0. Previously we have shown that, because thermal expansion changes n, maps of the plasmon energy can be converted into temperature maps with nanometer-scale spatial resolution[22]. Such plasmon energy maps can also reveal the electron wind force, which puts some parts of a current-carrying wire into compression (raising the density) and others into tension (lowering the density).

Experiment

We demonstrate this technique on a 1.1 μm-long aluminum nanowire fabricated with e-beam lithography on a 20 nm-thick silicon nitride membrane (Figs. 1 and S1). The experiment is essentially an accelerated lifetime test, where our chosen bias current is large, but still small enough that the expected time-to-failure is long compared to the length of the experiment. Imaging the nanowire in unbiased and biased states while collecting an EELS spectrum at every xy pixel produces a spectrum image for each condition. Fitting the spectra provides an xy map of the sample in each fit parameter (Figs. S13–S17). These maps can be further manipulated to extract physical parameters. For instance, comparing the intensity in the aluminum plasmon to the intensity of the zero-loss peak (ZLP) gives an xy map of the device thickness (Fig. 1C,D). Averaged over its length L, the nanowire's trapezoidal altitude profile is approximately parabolic with a base $b = 50$ nm, a height $h = 30$ nm, and a cross-sectional area $A = (2/3)bh = 1000$ nm^2.

The most pertinent fit-parameter maps show the center energy E_p of the Al bulk plasmon

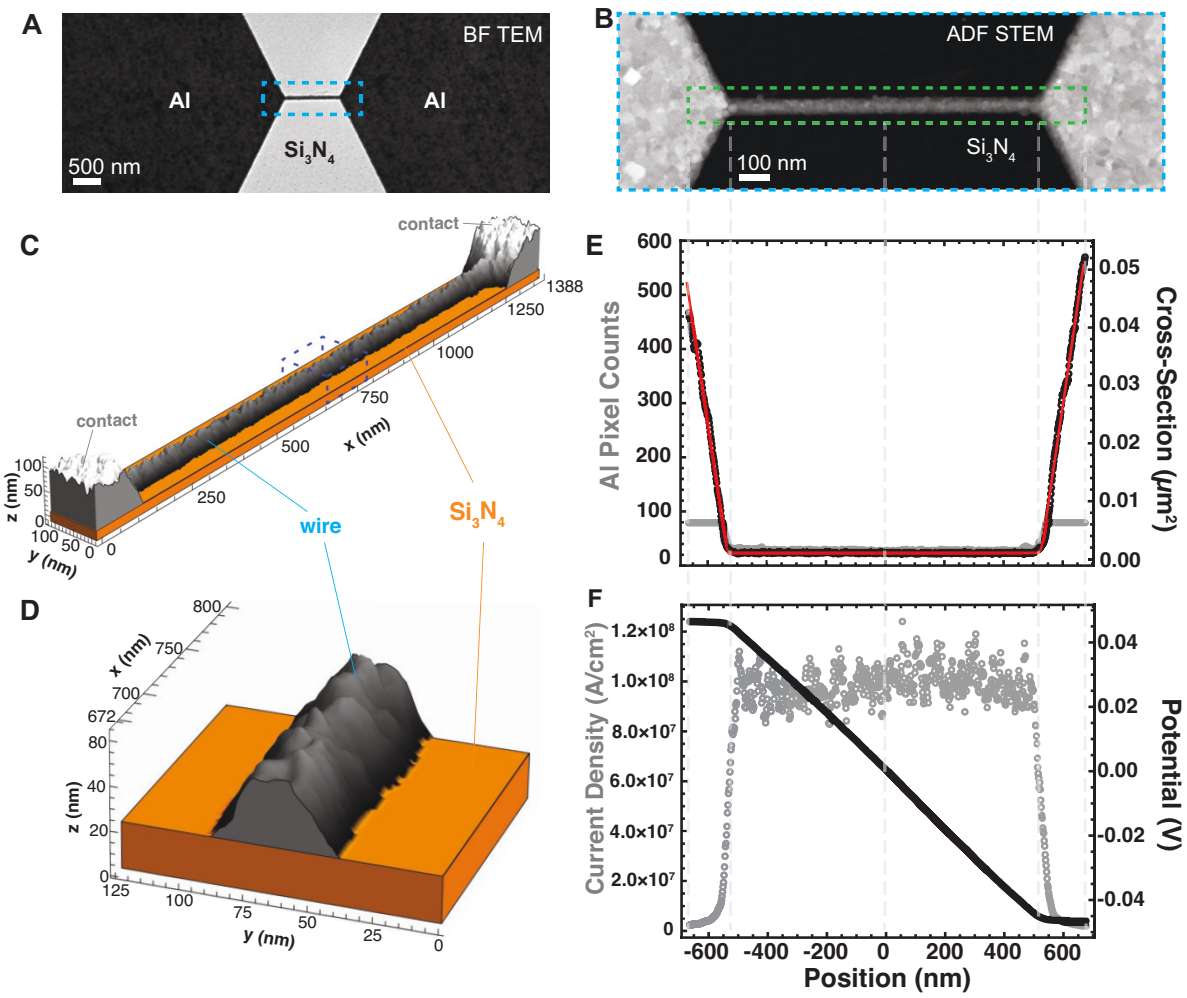

Figure 1: **Experiment setup:** **(A)** and **(B)** bright-field (BF) TEM and annular dark field (ADF) STEM images, respectively, of an aluminum nanowire. **(C)** Thickness of the aluminum nanowire, as determined by the EELS plasmon ratio method (see Eq. S3). **(D)** Detail of the region indicated by the dashed frame in (C). **(E)** The nanowire's width in 1.7 nm pixels in the spectrum image (green dashed region in (B)), and the nanowire's cross section A as determined by integrating its thickness over its width (fit shown in red). Where the width is clipped by the spectrum image's field of view, its value is extrapolated (Fig. S9). **(F)** The current density and electrical potential as a function of position along the wire (Fig. S9) for the experiment of Fig. 2B. Parts (B), (E), and (F) share the same horizontal axis. The position and potential origins have been chosen to be at the center of the wire.

(Fig. 2). We bias the nanowire *in situ* with 0, 100, 0, 100, and 0 μW dissipation in the nanowire, where the bias current polarity is positive and negative for the 2nd and 4th spectrum images, respectively. The spectrum images are acquired sequentially with an acquisition time of 42 minutes per spectrum image, with no more than 6 minutes between each map. At non-zero bias the nanowires anneal under the influence of the current density J of 10^8 A/cm^2, reducing the nanowire resistance by 10% over the course of a spectrum image. Feedback holds the power dissipation (and thus the temperature) constant, so the magnitude of the average current I for the negative polarity (-1.07 mA) is 4% larger than that of the positive polarity ($+1.03$ mA).

The plasmon energy maps (Fig. 2) show grain boundaries both in the nanowire and in the contacts, demonstrating that the xy spatial resolution and the E_p energy sensitivity are sufficient to see such atomic-scale density variations[22]. In the 1st scan, the plasmon energy is uniform (excepting the grain boundaries) across both contacts and the nanowire, which indicates that the unbiased wire is unstrained.

In the 2nd scan ($+$ bias), the plasmon energies are no longer spatially uniform. Relative to zero bias, they increase in the left half of the wire and decrease in the right half of the wire. These shifts imply that the wire's left half is becoming denser while its right half is becoming less dense. The 3rd scan produces a plasmon energy map that is similar — but not identical — to the 1st. The 4th scan ($-$ bias) again creates plasmon energy variation across the nanowire, but this time the plasmon energy decreases in the left half of the wire and increases in the right half of the wire. The 5th and final scan shows a plasmon energy distribution that is similar to that of the 1st and 3rd scans. Averaging the plasmon energy maps across the width of the nanowire gives E_p line profiles that show good reproducibility among the zero bias measurements. The line profiles from the '$+$' and '$-$'-biased nanowire differ from each other, and from the zero bias profiles.

Because of the bamboo grain boundary effect, narrower wires are generally more resistant to electromigration, so we expect a critical Blech product $(JL)_c \gtrsim 5000$ A/cm[2,7,10,23] for these 30-

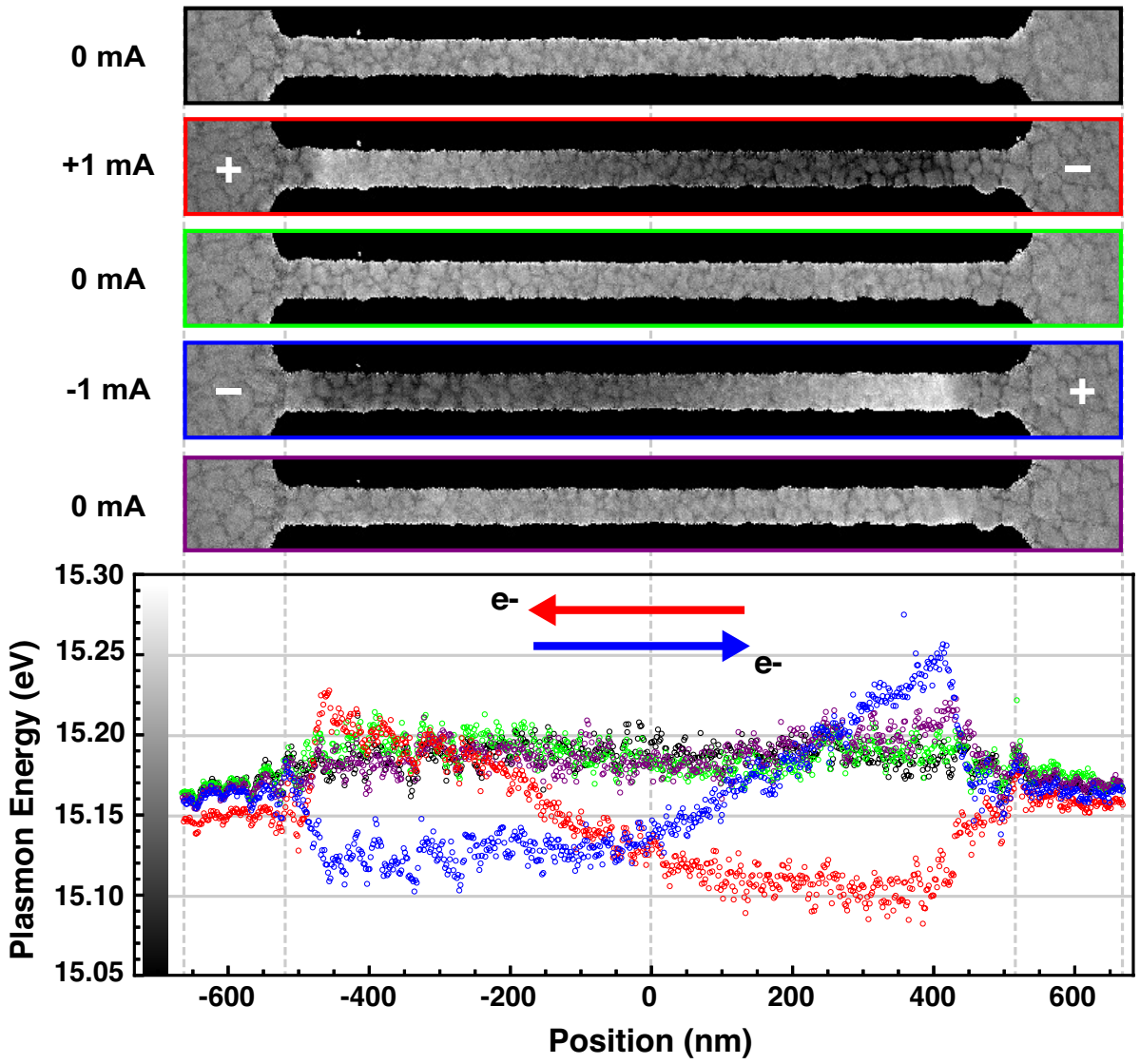

Figure 2: **Plasmon energy maps:** (top) Consecutive plasmon energy maps at five currents I: 0, $+1.03$, 0, -1.07, and 0 mA. (bottom) Line profiles generated by averaging across the shorter dimension in each map. The direction of the electron current is indicated. The maps are 795×74 pixels, and each pixel is 1.7 nm on a side.

nm-tall wires at $T \lesssim 100°$C. However, the current density $J \simeq 1.0 \times 10^8$ A/cm^2 is large enough to put this $L = 1.1\ \mu$m nanowire at least near the threshold length. Thus some electromigration, and possibly even eventual failure, is expected. The 10% resistance drops are clear evidence that atomic migration occurs. In fact, careful analysis of the zero-power spectrum images shows the movement of aluminum atoms in two distinct ways. First, the thickness of the aluminum, as determined by the ratio of the plasmon peak to the ZLP, is systematically altered by the application of the electrical current. At positive bias the left-hand side of the wire becomes thicker while the right-hand side becomes thinner (Fig. S19). These changes reverse when the current polarity reverses; in both cases aluminum is moving from the cathode toward the anode. Second, the zero-power density of the aluminum, as determined by the plasmon energy, has increased on the left-hand (right-hand) side of the wire after positive (negative) applied bias, which again indicates cathode-to-anode motion of the aluminum (Figs. S15 and S20). Interpreting these two effects in terms of atomic currents, we see that the thickness-changing current is about $100\times$ larger than the density-changing atomic current (Fig. S21).

The successive zero-bias plasmon energy maps are almost indistinguishable compared to the $\pm$-biased plasmon energy maps, which are very different from each other and from the zero-bias maps. The enduring, or plastic, effect on the wire density is thus small in comparison to the transient elastic effect. While the atomic current responsible for the enduring density changes might cause the wire to fail eventually, here the 46–49 minute periods with the current applied (slightly longer than the scan time) are short enough that the back-stress field created by atomic motion does not develop substantially. In other words, because the spectrum images show that the wire is relatively unchanged from its initial configuration after the applied ± 1 mA has been reduced to zero, we can conclude that the time-integrated effect of the atomic currents on the back-stress is so small as to be negligible in comparison to the prompt response to the electron wind force. The mass transport's integrated effect on the atomic density is thus negligible in comparison to the transient effect created by the bias current.

Analysis

We understand the plasmon energy's transient response to the bias current $I = JA$ in terms of two distinct effects that occur on sub-second timescales: Joule heating ($\propto J^2$) and the electron wind force ($\propto J$). The Joule heating ρJ^2 (ρ is the resistivity) produces thermal expansion and a concomitant density change that is both an even function of the applied current and an even function of position about the wire midpoint. With an effective ionic charge $Z^* < 0$ the wind force $F_{\text{wind}} \equiv Z^* eE = Z^* e\rho J$ (E is the electric field) pushes the aluminum atoms in the direction of the electron flow, putting the upstream side of the nanowire into tension and the downstream side of the nanowire into compression. This second density-changing effect is an odd function of the applied current and an odd function of position about the wire midpoint. Although both effects are present simultaneously, they can be separated via their different symmetries under the current reversal.

We take the electron density $n = n_0 + \Delta n$, where Δn is the shift of n relative to its unperturbed value n_0. Expanding Eq. 1 in a Taylor series, we then construct maps of the ratio $R \equiv (E_p - E_{p0})/E_{p0} \simeq \Delta n/2n_0$, where the reference, zero-bias plasmon energy map E_{p0} is the one acquired directly after the E_p map acquired under bias. From the positive-current map $R(+I)$ and the negative-current map $R(-I)$ we then construct $R(+I) + R(-I) \simeq \Delta n_{\text{even}}/n_0$ and $R(+I) - R(-I) \simeq \Delta n_{\text{odd}}/n_0$, where $\Delta n(\pm I) \equiv \Delta n_{\text{even}} \pm \Delta n_{\text{odd}}$ and Δn_{even} and Δn_{odd} are the current-even and current-odd shifts of the electron density n, respectively (Fig. 3). The temperature-dependent coefficient of linear thermal expansion $\alpha(T)$ and Δn_{even} give the wire temperature T as described previously[22], while the bulk modulus B and Δn_{odd} give the pressure in the wire $P = 3B\Delta n_{\text{odd}}/n_0$ (Eq. S10b).

Discussion

Spectra acquired at 40 Hz within a grain in the contacts measure the plasmon energy with a standard deviation of 10 meV, which corresponds to a fractional precision of 0.0006. This

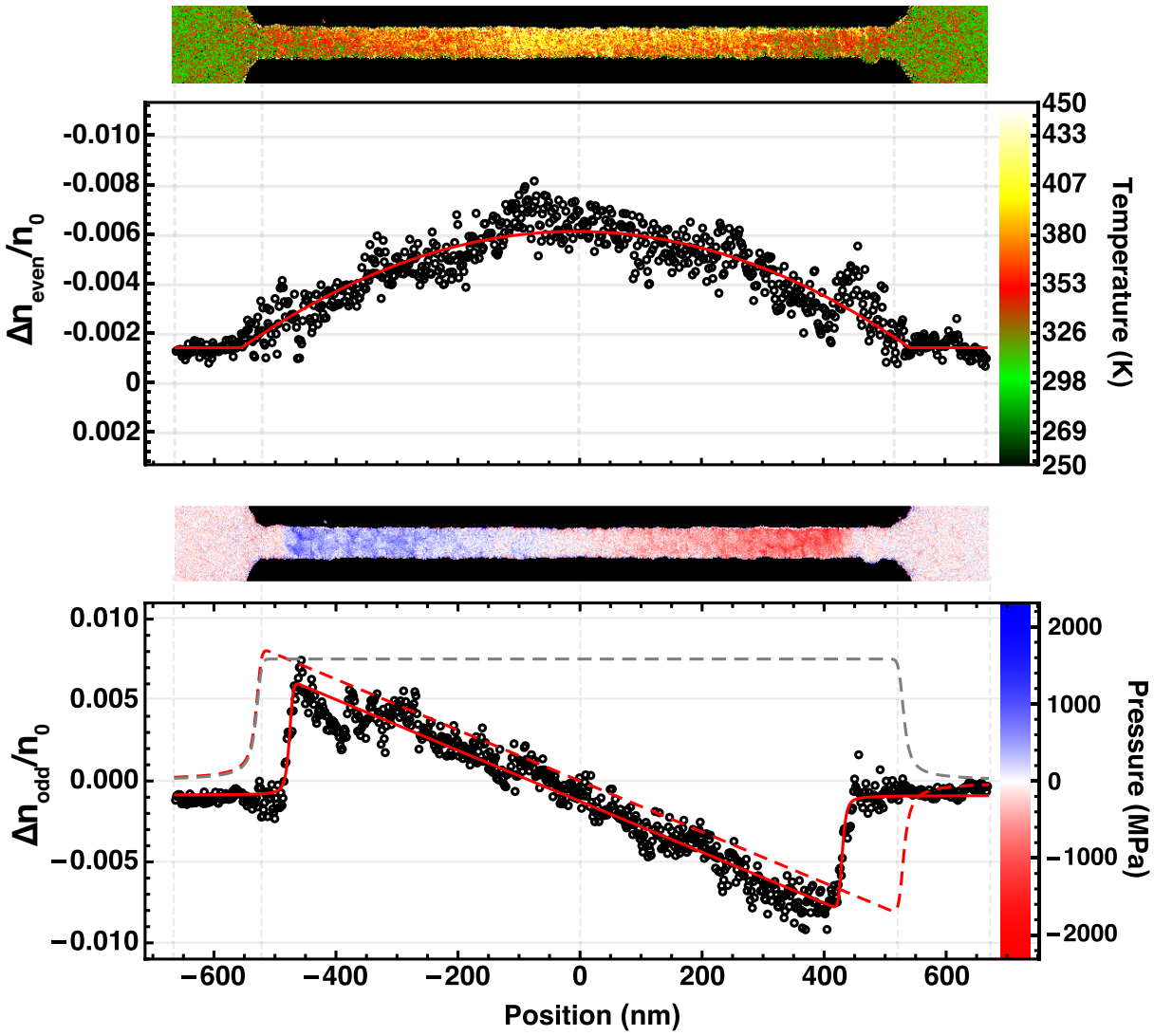

Figure 3: T **and** P **separation by symmetry under current reversal:** Relative plasmon energy shifts (Fig.2), when added and subtracted according to the sign of the applied current, give the current-even and current-odd relative shifts of the electron density n (left axes). Aluminum's density varies with temperature T and applied pressure P according to simple relations parametrized by thermal expansion coefficients and the bulk modulus. Inverting these relations gives the local T and P (right axes), which have their spatial (x) dependence fit to analytic functions (solid red curves). The lower plot also shows the x-dependence of the current density J (grey dashed curve) and the corresponding (i.e. expected) pressure profile (red dashed curve). The measured pressure profile turns over sooner and more abruptly (Fig. S10) than expected for $P \propto xJ$ (Eq. 2).

statistical precision in turn corresponds to a temperature sensitivity of 3 K/$\sqrt{\text{Hz}}$ and a pressure sensitivity of 60 MPa/$\sqrt{\text{Hz}}$. For comparison, a pressure-imaging technique that interrogates nitrogen-vacancy color centers in the culet of a diamond anvil cell has recently achieved a pressure sensitivity of 20 MPa/$\sqrt{\text{Hz}}$[24]. This technique queries the diamond neighboring the sample with a laser beam and achieves a spatial resolution of $\sim 5\,\mu$m. Here we query the aluminum sample itself with an electron beam and achieve a spatial resolution ~ 3 nm[22].

The density shifts Δn_{even} and Δn_{odd} show the even and odd symmetry about the $x = 0$ mid-plane, respectively, that is expected for Joule heating $\propto J^2$ and an electron-wind force $\propto J$[3,25]. Moreover, some details corroborate our expectations for the underlying physics. The temperature profile is peaked in the center, away from the thermal sinks provided by the contacts, and can be approximated with a parabola or cosine (Eq. S6). The pressure is such that the electron 'wind' pushes material toward the anode. Its profile $P(x)$ is linear for some 80% of the wire's length, with the pressure zero at the nanowire midpoint, and from its extrema it transitions back to its zero value near the ends of the nanowire. This behavior can be understood by considering the effect of the wind force F_{wind} on an elastic wire (Eq. S15), with the result

$$P(x) = \frac{Z^* e \rho}{\Omega} x J(x), \tag{2}$$

where Ω is the atomic volume and the other parameters have been defined previously. This system is somewhat like an elastic rod, supported above and below, in a gravitational field (Fig. S7), but here the applied force scales like $1/A$ as a function of the rod's cross sectional area A; as the wire widens into the contacts the (wind) force decreases with the current density J while the nanowire's effective (1D) stiffness increases $\propto A$. This spatial dependence $P(x) \propto xJ(x)$ for the *plastic* stress has been anticipated for decades[5,9,26], and the elastic stress's profile would be expected to be similar. Assuming electrons are the charge carriers, fitting the observed $P(x)$ to Eq. 2 gives a value $Z^* = -4$ for the effective ionic charge. This value is consistent with previous reports[26] and indicates that the 'wind' force due to momentum transfer from electrons dominates the 'direct' force due to the applied electric field[3]. While larger than the

yield strength of bulk aluminum, the observed pressures of 1–2 GPa are reasonable given that the Hall-Petch effect greatly increases the strength of nanocrystalline aluminum[27] and that a typical grain size in this wire is about one-third of the wire thickness.

However, other details do not corroborate our expectations. The classical wind force model (Eq. 2) predicts that the pressure extrema occur where the nanowire widens at the contacts, whereas the extrema are observed well inside the wire, some two wire-diameters away from the contacts. This discrepancy is not understood, but with this STEM-EELS-based technique the effect is gross and well-resolved spatially. The position of greatest wind-force tension — i.e. the point of most probable electromigration-induced failure — is located 100 nm from where it might otherwise be expected. Moreover, the length scale over which the pressure profile returns from the extrema to the ambient is $6\times$ shorter than the value expected based on the 63° contact-opening half-angle (Fig. S10). Experimental limitations due to, for example, finite resolution[22] and spatial averaging generally blur sharp transitions, which makes this enhancement especially surprising. These unexpected features of the short-length effect point to new physics. While presently not understood, the operative mechanism is protective against electromigration, independent of the plastic back-stress underlying the traditional Blech effect, and might be dominant in wires $\lesssim 100$ nm long. As the transistor pitch in the current semiconductor fabrication technology nodes is only a few tens of nanometers, the first metallization layers in a microprocessor contain billions of wires below this threshold. Thus a more complete understanding of this effect might lead to a revolutionary new set of electromigration countermeasures for IC design.

Associated Content

Supporting Information

Methods, spectrum image data summary, details of atomic current analysis, and Supporting Figures S1–S21. The Supporting Information is available free of charge on the ACS Publications website at DOI: 10.1021/acs.nanolett.xxx.

Author Information

Corresponding Author

* (M.H.M.) E-mail: Matthew.H.Mecklenburg@aero.org.

Notes

The authors declare no competing financial interest.

Acknowledgments

We acknowledge fruitful discussions with Jared J. Lodico and Bernhard Schafer. We also thank Toshihiro Aoki at UCI and Arda Genç and Joerg Jinschek at ThermoFischer Scientific for their assistance. This work was supported by the Semiconductor Research Corporation (SRC), by National Science Foundation (NSF) awards DMR-1611036 and DMR-2004897, by NSF STC award DMR-1548924 (STROBE), and by The Aerospace Corporation's SERPA program. Devices were fabricated in the Integrated Systems Nanofabrication Cleanroom (ISNC) at the California NanoSystems Institute (CNSI). TEM imaging and spectroscopy were performed at USC's Core Center of Excellence in Nano Imaging (CNI).

References

[1] Ceric, H. & Selberherr, S. Electromigration in submicron interconnect features of integrated circuits. *Materials Science and Engineering R: Reports* **71**, 53–86 (2011).

[2] Lienig, J. & Thiele, M. *Fundamentals of Electromigration-Aware Integrated Circuit Design* (Springer International Publishing, Cham, 2018).

[3] Tu, K. N. *Solder Joint Technology : Materials, Properties, and Reliability*. Springer Series in Materials Science (Springer, New York, 2007).

[4] International Roadmap for Devices and Systems. Executive Summary 2020, IEEE (2020).

[5] Bigalke, S., Lienig, J., Jerke, G., Scheible, J. & Jancke, R. The need and opportunities of electromigration-aware integrated circuit design. In *Proceedings of the International Conference on Computer-Aided Design*, ICCAD '18, 1–8 (Association for Computing Machinery, New York, NY, USA, 2018).

[6] Tu, K., Liu, Y. & Li, M. Effect of Joule heating and current crowding on electromigration in mobile technology. *Applied Physics Reviews* **4**, 011101 (2017).

[7] Blech, I. A. Electromigration in thin aluminum films on titanium nitride. *Journal of Applied Physics* **47**, 1203–1208 (1976).

[8] Oates, A. S. The electromigration short-length effect and its impact on circuit reliability. In *2013 IEEE International Interconnect Technology Conference - IITC*, 1–3 (2013).

[9] Blech, I. & Herring, C. Stress generation by electromigration. *Applied Physics Letters* **29**, 131–133 (1976).

[10] Schreiber, H. U. Electromigration threshold in aluminum films. *Solid-State Electronics* **28**, 617–626 (1985).

[11] Okabayashi, H., Komatsu, M. & Mori, H. Depth-resolved in-situ TEM observation of electromigration in a submicron-wide layered Al–0.5% Cu line. *Japanese Journal of Applied Physics* **35**, 1102 (1996).

[12] Wang, P.-C., Noyan, I. C., Kaldor, S. K., Jordan-Sweet, J. L., Liniger, E. G. & Hu, C.-K. Topographic measurement of electromigration-induced stress gradients in aluminum conductor lines. *Applied Physics Letters* **76**, 3726–3728 (2000).

[13] Tamura, N., MacDowell, A. A., Spolenak, R., Valek, B. C., Bravman, J. C., Brown, W. L., Celestre, R. S., Padmore, H. A., Batterman, B. W. & Patel, J. R. Scanning X-ray microdiffraction with submicrometer white beam for strain/stress and orientation mapping in thin films. *Journal of Synchrotron Radiation* **10**, 137–143 (2003).

[14] Weide-Zaage, K., Dalleau, D. & Yu, X. Static and dynamic analysis of failure locations and void formation in interconnects due to various migration mechanisms. *Materials Science in Semiconductor Processing* **6**, 85–92 (2003).

[15] Nucci, J., Krämer, S., Arzt, E. & Volkert, C. Local strains measured in Al lines during thermal cycling and electromigration using convergent-beam electron diffraction. *Journal of Materials Research* **20**, 1851–1859 (2005).

[16] Takahashi, Y., Nishino, Y., Furukawa, H., Kubo, H., Yamauchi, K., Ishikawa, T. & Matsubara, E. Observation of electromigration in a Cu thin line by in situ coherent X-ray diffraction microscopy. *Journal of Applied Physics* **105**, 124911 (2009).

[17] Chen, K., Tamura, N., Kunz, M., Tu, K. N. & Lai, Y.-S. In situ measurement of electromigration-induced transient stress in Pb-free Sn–Cu solder joints by synchrotron radiation based X-ray polychromatic microdiffraction. *Journal of Applied Physics* **106**, 023502 (2009).

[18] Nam, S.-W., Chung, H.-S., Lo, Y. C., Qi, L., Li, J., Lu, Y., Johnson, A. T. C., Jung, Y., Nukala, P. & Agarwal, R. Electrical wind force-driven and dislocation-templated amorphization in phase-change nanowires. *Science* **336**, 1561–1566 (2012).

[19] Lin, S.-k., Liu, Y.-c., Chiu, S.-J., Liu, Y.-T. & Lee, H.-Y. The electromigration effect revisited: non-uniform local tensile stress-driven diffusion. *Scientific Reports* **7**, 1–10 (2017).

[20] Liang, C.-L., Lee, S.-W. & Lin, K.-L. The mechanism of an increase in electrical resistance in Al thin film induced by current stressing. *Thin Solid Films* **636**, 164–170 (2017).

[21] Liu, Y.-c., Lin, S.-k. & Chiu, S.-J. On the Schmid's Law for the electric current-induced deformation: An in situ EBSD study. *International Journal of Mechanical Sciences* **168**, 105295 (2020).

[22] Mecklenburg, M., Hubbard, W. A., White, E. R., Dhall, R., Cronin, S. B., Aloni, S. & Regan, B. C. Nanoscale temperature mapping in operating microelectronic devices. *Science* **347**, 629–632 (2015).

[23] Witt, C. *Electromigration in Bamboo Aluminum Interconnects*. Ph.D. thesis, Stuttgart, Stuttgart (2000).

[24] Hsieh, S., Bhattacharyya, P., Zu, C., Mittiga, T., Smart, T. J., Machado, F., Kobrin, B., Höhn, T. O., Rui, N. Z., Kamrani, M., Chatterjee, S., Choi, S., Zaletel, M., Struzhkin, V. V., Moore, J. E., Levitas, V. I., Jeanloz, R. & Yao, N. Y. Imaging stress and magnetism at high pressures using a nanoscale quantum sensor. *Science* **366**, 1349–1354 (2019).

[25] Liu, Y.-C. & Lin, S.-K. A critical review on the electromigration effect, the electroplastic effect, and perspectives on the effects of electric current upon alloy phase stability. *JOM* **71**, 3094–3106 (2019).

[26] Korhonen, M. A., Børgesen, P., Tu, K. N. & Li, C.-Y. Stress evolution due to electromigration in confined metal lines. *Journal of Applied Physics* **73**, 3790–3799 (1993).

[27] Farhat, Z. N., Ding, Y., Northwood, D. O. & Alpas, A. T. Effect of grain size on friction and wear of nanocrystalline aluminum. *Materials Science and Engineering: A* **206**, 302–313 (1996).

[28] Mkhoyan, K. A., Babinec, T., Maccagnano, S. E., Kirkland, E. J. & Silcox, J. Separation of bulk and surface-losses in low-loss EELS measurements in STEM. *Ultramicroscopy* **107**, 345–355 (2007).

[29] Malis, T., Cheng, S. C. & Egerton, R. F. EELS log-ratio technique for specimen-thickness measurement in the TEM. *Journal of Electron Microscopy Technique* **8**, 193–200 (1988).

[30] Gross, D., Ehlers, W., Wriggers, P., Schroder, J. & Muller, R. *Mechanics of Materials – Formulas and Problems* (Springer, Berlin, Germany, 2017).

[31] Comte, C. & von Stebut, J. Microprobe-type measurement of Young's modulus and Poisson coefficient by means of depth sensing indentation and acoustic microscopy. *Surface and Coatings Technology* **154**, 42–48 (2002).

A Supporting Information for:

Visualizing the Electron Wind Force in the Elastic Regime

Matthew Mecklenburg,[1,2] Brian T. Zutter,[3,4] Xin Yi Ling[3],

William A. Hubbard,[3,4] B. C. Regan[3,4]

[1]*Core Center of Excellence in Nano Imaging (CNI), University of Southern California, Los Angeles, CA, 90089, U.S.A*
[2]*Microelectronics Technology Department, The Aerospace Corporation, Los Angeles, CA, 90009, U.S.A*
[3]*Department of Physics and Astronomy, University of California, Los Angeles, CA 90095, U.S.A*
[4]*California NanoSystems Institute, University of California, Los Angeles, CA 90095, U.S.A*

Contents

Figures

A.1 Methods

A.1.1 Hardware

Unless otherwise noted, data are acquired using a JEOL JEM-2100F TEM (accelerating voltage 80 kV, beam current 300 pA, and probe convergence angle $\alpha = 12$ mrad) and a Gatan Quantum 963 GIF spectrometer (collection angle $\beta = 17$ mrad). The zero-loss peak (ZLP) full-width at half max (FWHM) of 0.6 eV is achieved by lowering the emission current to 50 μA and carefully adjusting the high tension ripple filters. Typical spectrum images (e.g. those used to generate Fig. 2) have a dwell time of 27 ms/pixel and spend 30% of the total image acquisition time performing drift correction. Acquiring a high quality dark reference after each spectrum image improves the quality of the spectra. The sample is contacted with an *in situ* biasing holder from Hummingbird Scientific and biased with a Keithley Model 2400 sourcemeter controlled with National Instruments' LabVIEW software.

A.1.2 Device architecture

STEM-compatible substrates are fabricated by etching with KOH through a 200 μm-thick, $\langle 100 \rangle$-oriented, double-sided-polished silicon wafer to reveal a 20 nm-thick, LPCVD-grown, silicon nitride membrane. Optically-defined Ti/Pt (5 nm/25 nm) leads terminate near the window edges. Aluminum nanowires with connections to the Ti/Pt leads for 4-wire measurements are patterned using e-beam lithography (Fig. S1) and e-beam evaporation. High-resolution STEM imaging (Fig. S2) shows that the aluminum is polycrystalline. Core loss EELS of the nanowires shows the elements Al, O, N, and Si in their expected locations (Fig. S3).

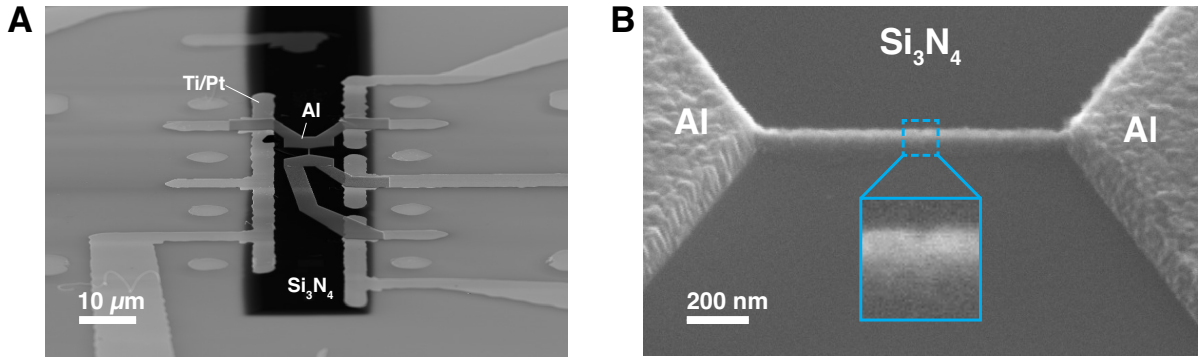

Figure S1: **Device architecture: (A)** A silicon chip supporting an electron-transparent silicon nitride membrane and supplied with Ti/Pt (5 nm titanium adhesion layer under 25 nm of platinum) optically-defined leads serves as the device substrate. On the membrane, which appears black in this SEM image, an aluminum nanowire is defined with a 4-wire topology using e-beam lithography. **(B)** An SEM image acquired with a 45° tilt shows the wire in profile. Shadowing by the e-beam resist produces a wire that has a cross-section that is roughly trapezoidal or parabolic. The wire's maximum thickness is one third of the nominal film thickness.

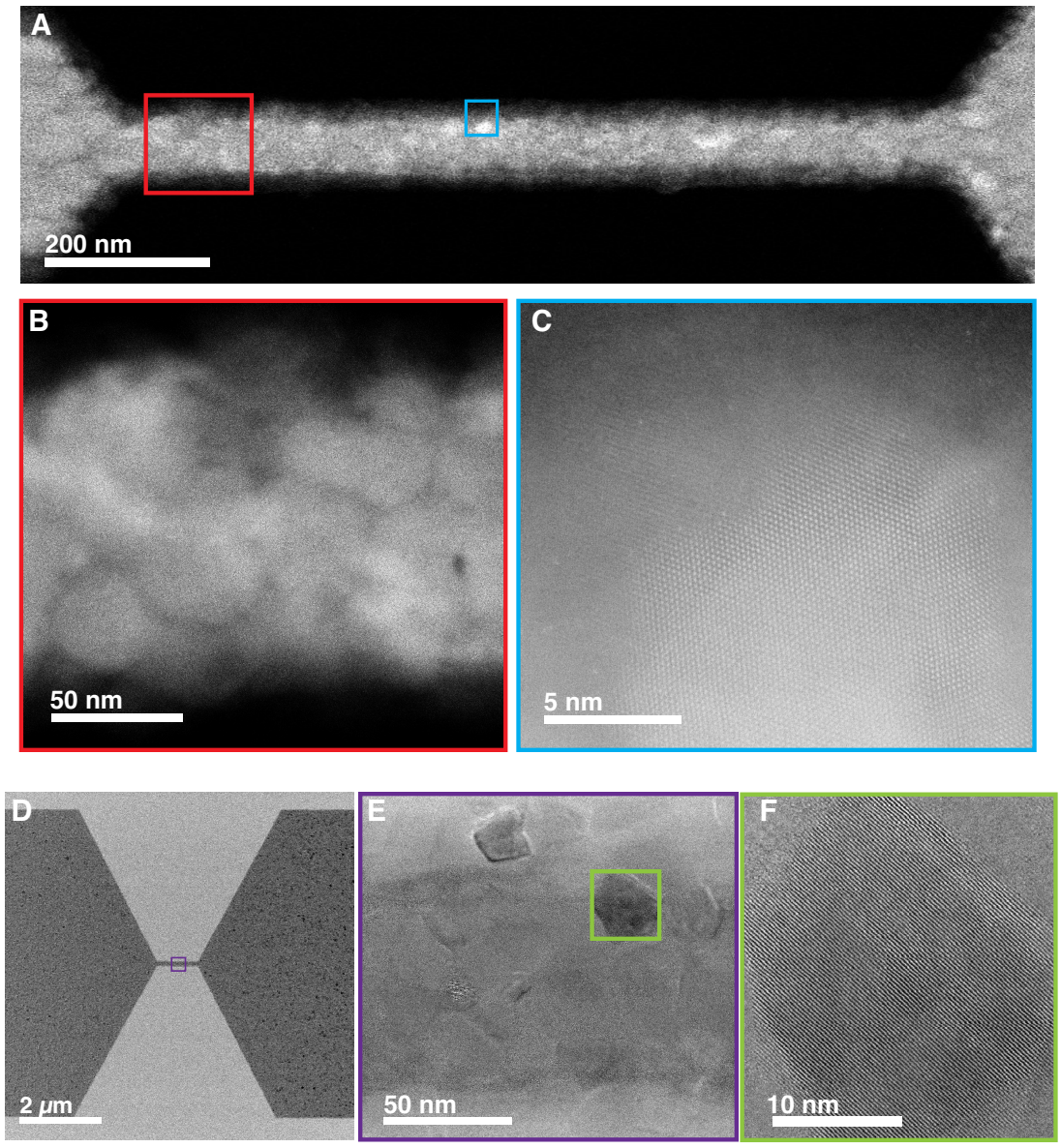

Figure S2: **STEM images of an Al nanowire:** Annular dark field (ADF, **A–C**) and bright field (BF, **D–F**) images show a representative, 150-nm-wide nanowire's structure at different levels of magnification. Images **C** and **F** show the aluminum lattice inside individual grains. Because the grains are randomly oriented, only some happen to be oriented near a zone axis, and thus not every grain shows crystallinity. We assume that each grain is crystalline and that this structure also occurs in our 50-nm-wide aluminum nanowires. These images were acquired with the JEOL Grand ARM 300CF in the Materials Research Institute (MRI) at the University of California, Irvine (UCI), using an accelerating voltage of 300 kV.

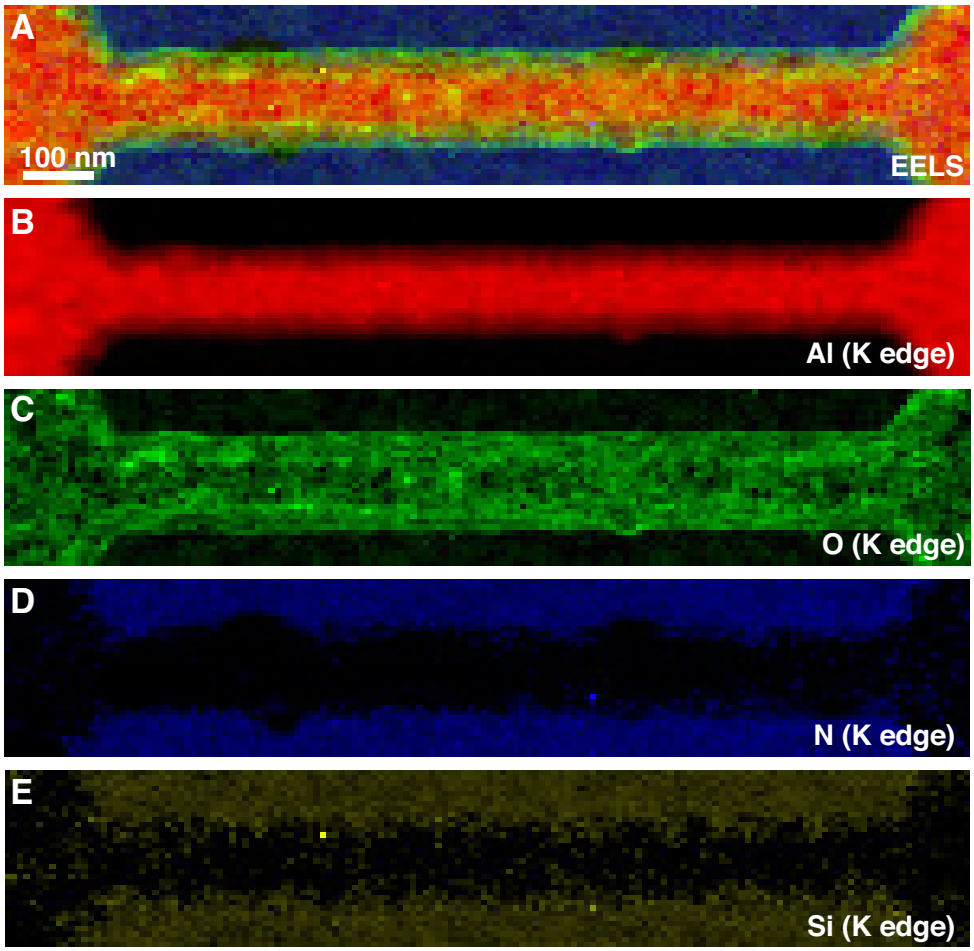

Figure S3: **Core-loss EELS mapping of an Al nanowire:** Performing EELS in the core loss regions of Al, O, N, and Si produces individual elemental maps (B–E, respectively) of the 1000 nm $\times$ 150 nm nanowire of Fig. S2, along with a combination image (A). The aluminum signal (B) gets progressively smaller as the film gets thinner moving from the contacts to the center of the nanowire to the edges. The nanowire's oxide coating (C) is uniform and makes a $\sim$ 10 nm contribution to the nanowire's physical width. The thin silicon nitride support membrane gives weak but discernible nitrogen (D) and silicon (E) signals. These images were acquired with the JEOL Grand ARM 300CF in the MRI at UCI using an accelerating voltage of 300 kV.

A.1.3 EELS fitting

To identify regions where the aluminum plasmon can be successfully fit, we perform a simple threshold test on the energy range 11–18.5 eV. Because the silicon nitride support membrane spans the entire field of view, the broad Si_3N_4 plasmon (FWHM 12.6 eV) centered at 23 eV produces a background that increases with increasing energy across the entire test range. If the signal below 16 eV never exceeds the maximum in this background, which occurs near 18.5 eV, then the aluminum plasmon is not large enough to fit. Therefore, if the maximum value in this range occurs below 16 eV, we fit the aluminum plasmon in the range 13.75–16.6 eV (Fig. S4), otherwise we categorize this region as having a negligible amount of aluminum. We estimate that this procedure correctly identifies any pixel containing an aluminum thickness greater than 2 nm, and many that have substantially less (Fig. S5). The wire boundaries identified by this threshold method also agree, to within a pixel or two, with those identified with methods that are not specific to elemental aluminum, namely ADF imaging and ZLP intensity mapping.

Fit parameter maps are extracted by fitting each spectrum $I(j)$ in an EELS spectrum image (Fig. S4). The ZLP is fit with a Gaussian function

$$I(j) = \frac{I_0 \Delta_{\text{bin}}}{\sqrt{2\pi\sigma^2}} \exp\left[-\frac{(j\Delta_{\text{bin}} - \mu_{\text{ZLP}})^2}{2\sigma^2}\right], \tag{S1}$$

where j is the bin number, I_0 is the total counts under the peak, $\Delta_{\text{bin}} = 0.025$ eV is the spectrometer bin width, σ parametrizes the ZLP width, and μ_{ZLP} is the center value. The plasmon peak is fit with a Lorentzian function

$$I(j) = \frac{I_1 \Delta_{\text{bin}}}{\pi} \frac{\Gamma/2}{(j\Delta_{\text{bin}} - \mu_{\text{pl}})^2 + (\Gamma/2)^2} + A_1 + A_2 j \Delta_{\text{bin}}, \tag{S2}$$

where I_1 is the total counts under the peak, Γ parametrizes the plasmon peak width, μ_{pl} is the center value, and $A_1 + A_2 j \Delta_{\text{bin}}$ parametrizes a linear background. To facilitate comparisons between the peak widths, we plot $\text{FWHM}_{\text{ZLP}} = (2\sqrt{2\ln 2})\sigma$ and $\text{FWHM}_{\text{pl}} = \Gamma$.

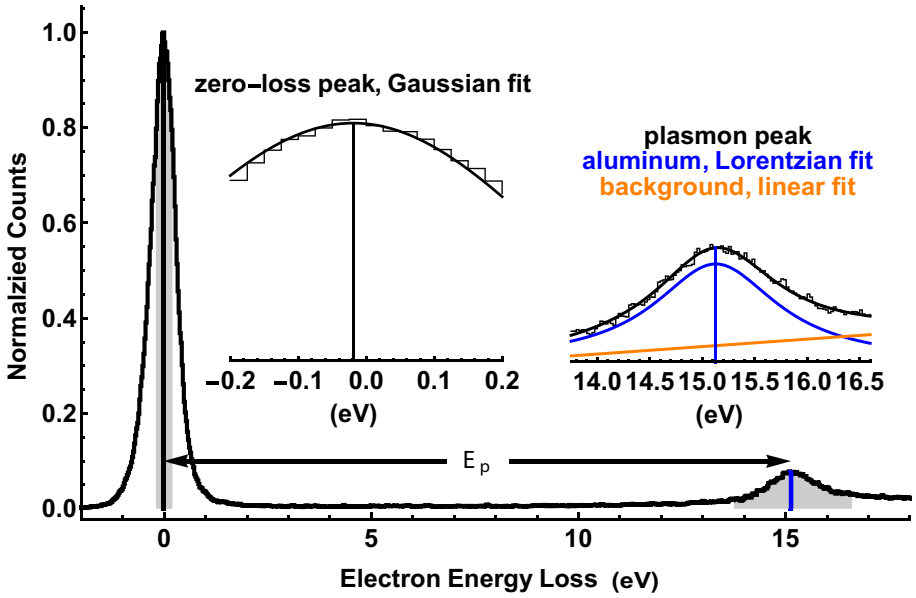

Figure S4: **Fitting an EELS spectrum:** A single EELS spectrum (one of 64000 in each spectrum image) is shown normalized such that the ZLP maximum is unity. Gray bands indicate the fit regions for the ZLP and the plasmon peak, and the vertical black and blue lines indicate the peak center values. The difference between the plasmon center and ZLP center is defined to be the plasmon energy. Insets show the fit regions for the ZLP and the plasmon peak in more detail. The former is fit to a Gaussian function (Eq. S1) and the latter is fit to a Lorentzian function with a linear background (Eq. S2).

A.1.4 Thickness determination

Using fit parameters extracted from an EELS spectrum we can estimate the sample thickness in two different ways, both of which assume that plasmons are created in a Poisson process. The plasmon ratio method[22,28], $t_{\mathrm{Al}}/\lambda_{\mathrm{Al}} = I_1/I_0$, gives the aluminum thickness t_{Al} in terms of the ratio of the first plasmon peak intensity I_1 to the ZLP intensity I_0, while the log-ratio method[29], $t/\lambda = \ln[I_t/I_0]$, gives the total thickness t of the sample in terms of the total intensity I_t and the ZLP intensity. These thickness determinations give consistent results with small spectrometer collection angles β and large Δ_{bin}. However, we use large β to maximize the count rate and small Δ_{bin} to maximize the precision of the plasmon energy fit.

At large β the ratio method underestimates the aluminum thickness because, due to elastic scattering into the first order Bragg reflections, the ZLP intensity increases faster than the plasmon peak intensity with increasing β. With increasing β the plasmon peak also gains intensity as the spectrometer captures more electrons that have created plasmons with non-zero momentum, but this effect is smaller and incompletely reflected in the fits, which assume a symmetric plasmon peak. (The plasmons' dispersion adds a high-energy shoulder to the plasmon peak.)

While the log-ratio method is thus potentially more accurate than the plasmon ratio method, it is difficult to accurately estimate the total intensity I_t when the full extent of the captured spectrum is less than 52 eV. Since we need the small $\Delta_{\mathrm{bin}} = 0.025$ eV to fit the plasmon precisely and the spectrometer has only 2048 bins, we correct for the error in the ratio method by applying a multiplicative factor of 1.42, which is determined by auxiliary measurements on the same samples with $\Delta_{\mathrm{bin}} = 0.1$ eV. For instance, on the silicon nitride we might find $\ln[I_t/I_0] = 0.35$, and on the contacts we might find $\ln[I_t/I_0] = 1.53$ and $I_1/I_0 = 0.83$. We estimate the actual thickness t_{Al} as

$$t_{\mathrm{Al}} = 1.42(I_1/I_0)\lambda_{\mathrm{Al}}, \tag{S3}$$

taking $\lambda_{\mathrm{Al}} = 72$ nm[29]. The absolute accuracy of the thickness determination is only fair (this

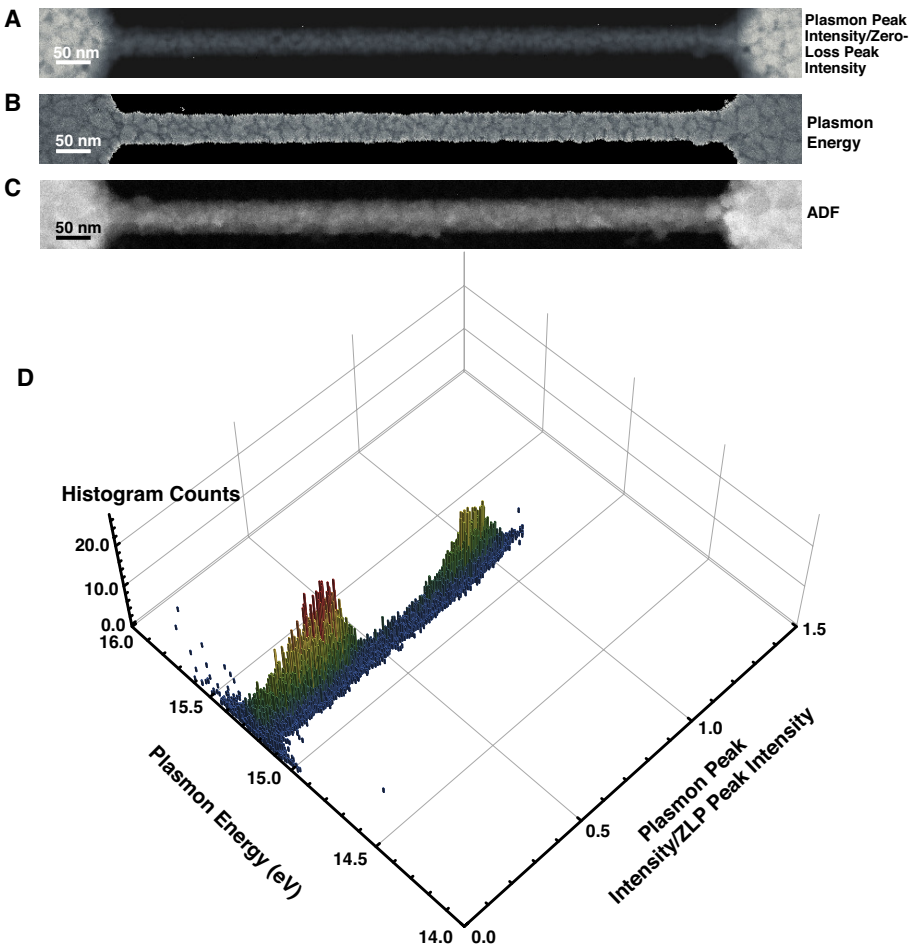

Figure S5: **Bulk plasmon center energy is insensitive to thickness: (A)** The ratio of the intensities of the plasmon peak to the ZLP shows that the aluminum film's thickness is nonuniform (see also Figs. 1, S1, and S9). **(B)** In contrast, the plasmon energy image shows that, aside from changes at grain boundaries, the plasmon energy does not vary along either the transverse or longitudinal direction in the wire. **(C)** The ADF image also shows the thickness variation, although less quantitatively than the intensity ratio map (A). **(D)** A double histogram plot of the images (A) and (B) shows the number of counts (z) as a function of thickness (x) and plasmon energy (y). Despite a $\sim 100\%$ variation in thickness, the plasmon energy typically varies by $< 0.1\%$. Most of this small variation is not noise, but rather the result of the decreased electron densities at grain boundaries[22]. The histogram shows two distinct humps; the larger one comes from the wire, and the smaller one comes from the contacts.

example gives $t_{\mathrm{Al}} = 85$ nm, when the film's nominal thickness is 100 nm), but the good point-to-point reproducibility of the measurements indicates that they provide precise values of relative thickness from scan to scan. We note in passing that the bulk plasmon's center energy is admirably insensitive to the film thickness (Fig. S5). This insensitivity is a key factor for allowing the use of the plasmon center energy as a clean, precision probe of both temperature and pressure (i.e. the wind force).

A.1.5 Profile analysis: temperature

We understand the aluminum wire's temperature profile $T(x)$ in terms of the time-independent heat equation with a Joule-heating source term,

$$\kappa \frac{\partial}{\partial x}\left(A\frac{\partial T}{\partial x}\right) = -EJA = -\frac{I^2\rho}{A}, \tag{S4}$$

where κ is the thermal conductivity, A is the wire's cross-sectional area, I is the current in the wire, and ρ is the wire's resistivity. By considering the profile as a function of one spatial dimension x only, we are neglecting the thermal conductivity of the silicon nitride membrane. To arrive at analytic expressions, we further take A to be constant in the wire and the contacts to be heat-sunk at temperature T_0. While both κ and ρ change with temperature, allowing both to vary makes Eq. S4 non-linear. The temperature dependence of ρ is more important, so we neglect the temperature dependence of κ and take

$$\rho = \rho_0(1 + (T - T_0)/T_\rho) = \rho_{\text{defect}} + \rho_{\text{bulk}}(1 + \alpha_{\text{TCR}}(T - T_0)), \tag{S5}$$

with the reference-temperature resistivity $\rho_0 = \rho_{\text{defect}} + \rho_{\text{bulk}}$ having defect (e.g. surfaces and grain boundaries) and bulk (i.e. intrinsic) contributions. The temperature dependence is parametrized either by T_ρ or by the bulk temperature-coefficient-of-resistivity α_{TCR}. Then Eq. S4 can be solved for a wire of length L with the boundary conditions $T(\pm L/2) = T_0$ to give

$$T(x) = T_0 + T_\rho\left(\frac{\cos[(IR_0/V_0)(2x/L)]}{\cos[IR_0/V_0]} - 1\right), \tag{S6}$$

where $R_0 = L\rho_0/A$ is the wire's resistance at zero bias and $V_0 = \sqrt{4\rho_0\kappa T_\rho}$. This temperature profile peaks at the center of the wire ($x = 0$) and reduces properly to the constant ρ result $T(x) = T_0 + I^2RL/(8\kappa A)$ in the limit $T_\rho \to \infty$.

Integrating $\rho(T(x))/A$ across the wire gives the wire's total resistance, which via Ohm's law $V = IR$ in turn gives the total voltage drop across the wire V (not to be confused with the volume V),

$$V = V_0 \tan(R_0 I/V_0). \tag{S7}$$

Fitting the $I - V$ profile of the aluminum nanowire to this function (Fig. S6) provides values for R_0 and V_0.

A.1.6 Profile analysis: pressure

Hooke's law can be written[30]

$$\epsilon_x = \frac{1}{E_Y}\left[\sigma_x - \nu(\sigma_y + \sigma_z)\right] + \alpha\Delta T, \tag{S8a}$$

$$\epsilon_y = \frac{1}{E_Y}\left[\sigma_y - \nu(\sigma_z + \sigma_x)\right] + \alpha\Delta T, \text{ and} \tag{S8b}$$

$$\epsilon_z = \frac{1}{E_Y}\left[\sigma_z - \nu(\sigma_x + \sigma_y)\right] + \alpha\Delta T, \tag{S8c}$$

where ϵ is the strain, σ is the stress, E_Y is Young's modulus, ν is Poisson's ratio, and α is the coefficient of linear thermal expansion. For the wire we take the stress to be entirely due to the wind force along x, with $\sigma_y = \sigma_z = 0$. Summing Eqs. S8 then gives

$$\epsilon_x + \epsilon_y + \epsilon_z = \frac{\sigma_x}{3B} + 3\alpha\Delta T, \tag{S9}$$

where we have introduced the bulk modulus $B \equiv -V\frac{dP}{dV} = \frac{E_Y}{3(1-2\nu)}$. The trace of the strain tensor is equal to the fractional change in the volume $\frac{\Delta V}{V}$. Exchanging the volume V for the number density n with $\frac{\Delta V}{V_0} = -\frac{\Delta n}{n_0}$ and $\Delta n(\pm I) \equiv \Delta n_{\text{even}} \pm \Delta n_{\text{odd}}$ then gives

$$\frac{\Delta n_{\text{even}}}{n_0} = -3\alpha\Delta T \quad \text{and} \tag{S10a}$$

$$\frac{\Delta n_{\text{odd}}}{n_0} = -\frac{\sigma_x}{3B}, \tag{S10b}$$

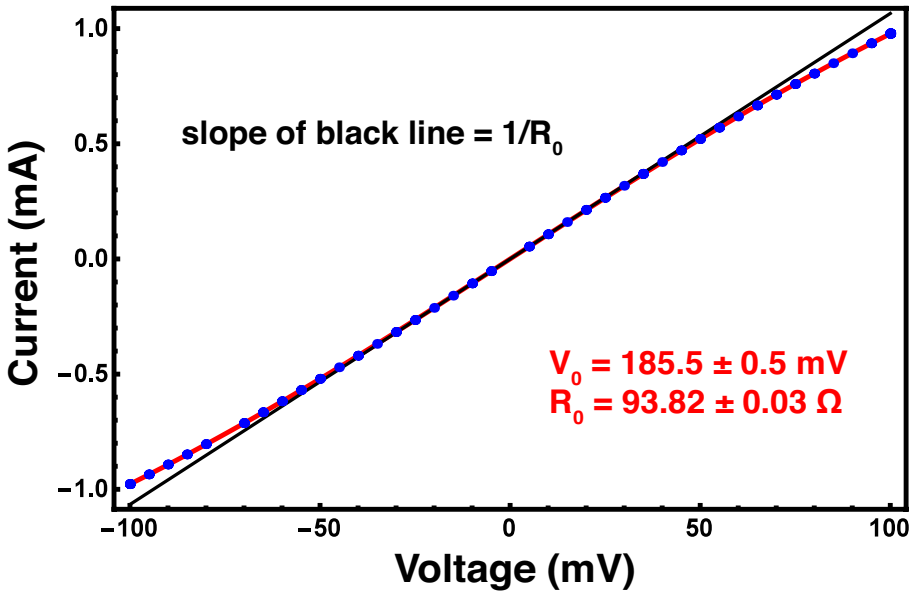

Figure S6: **Current-voltage ($I-V$) characteristic of the aluminum nanowire:** The data (blue, acquired immediately before the 2nd scan of Fig. 2) is fit (red) to $V = V_0 \sin(R_0 I/V_0)$ (Eq. S7), where $R_0 = L\rho_0/A$ is the resistance at zero bias and $V_0 = \sqrt{4\rho_0 \kappa T_\rho}$. When combined with the nanowire dimensions as determined using traditional STEM and STEM EELS ($L = 1063$ nm and $A = 1060$ nm^2, see Fig. S9), the fit value $R_0 = (93.82 \pm 0.03)\ \Omega$ gives an aluminum resistivity $\rho_0 = 9.4\ \mu\Omega$·cm. Given $\rho_{\text{bulk}} = 2.7\ \mu\Omega$·cm, this value implies $\rho_{\text{defect}} = 6.7\ \mu\Omega$·cm, a reasonable defect contribution given that the wire's radius is comparable to the electron mean free path in the bulk.

The fit parameter V_0 depends on the product κT_ρ, but these can be disentangled using the PEET determination of the temperature profile (Fig. 3) and Eq. S6, with the results $T_\rho = (600 \pm 100)$ K and $\kappa = (180 \pm 20)$ W/(m·K). These values in turn imply a $\alpha_{\text{TCR}} = 0.005$ K^{-1}, which is within 20% of the expected bulk value of 0.0043 K^{-1}. Note that during the T measurement the R_0 drops after the 1st, '+' bias to $(85.35 \pm 0.03)\ \Omega$, and after the 2nd, '−' bias to $(75.35 \pm 0.03)\ \Omega$ from the value determined in this $I-V$. These values for T_ρ, κ, and α_{TCR} are determined by applying the one T measurement to each of two results of the post-bias $I-V$ fits and then averaging the two results. To find the value for Z^* we take in Eq. 2 (Eq. S15) $\rho \simeq \rho_0$, where ρ_0 is the average of the two room-temperature resistivities determined by the fits to the post-bias $I-V$ measurements.

This combination of $I-V$ data with STEM imaging and precision low-loss STEM EELS gives a remarkably complete characterization of the nanowire. With only the bulk coefficient of thermal expansion $\alpha(T)$, bulk resistivity ρ_{bulk}, and bulk modulus B as inputs, we extract the nanowire's length L, width w, thickness t, room temperature resistivity ρ_0, defect contribution to the resistivity ρ_{defect}, temperature coefficient of resistivity α_{TCR}, thermal conductivity κ, and effective ionic charge Z^*, not to mention the maps detailing the local temperature and pressure everywhere.

where we have separated the two terms according to their distinct symmetries under reversal of the current I. These Eqs. S10 relate the quantities measured via the plasmon energy ratio R (not to be confused with the wire resistance R) to the temperature and pressure in the wire. We extract the temperature T from Eq. S10a, accounting for the temperature dependence of α as described in Ref. 22. Using Eq. S10b we find the pressure $P = -\sigma_x = 3B\Delta n_{\text{odd}}/n_0$, where positive (negative) P indicates compression (tension). The factor of three in the pressure formula can be understood as follows: because the wire is unstressed in the two directions orthogonal to the wire axis, to produce a given density change one requires $3\times$ the pressure required in the isotropic case. We use the values $E_Y = B = 70$ GPa and $\nu = 1/3$ for aluminum[31] in all calculations.

To find analytic expressions for the wire displacements and pressure gradients created by the electron wind force, we approximate the total potential energy U of the wire as

$$\begin{aligned} U &= \int \lambda dx \\ &= \int \left(\frac{1}{2} E_Y A \left(\frac{du_x}{dx} \right)^2 - \frac{1}{\Omega} F_{\text{wind}} u_x A \right) dx, \end{aligned} \tag{S11}$$

where the integral of the linear energy density λ extends over the contacts and the length L of the wire, which has its axis oriented along the x-direction. The first term on the second line of Eq. S11 represents the elastic strain energy in the wire. This energy arises via Hooke's law $\sigma_x = E_Y \epsilon_x$ (Eq. S8a), where we are now neglecting thermal effects. The strain in turn is related to the displacements $u_x(x)$ by $\epsilon_x = \frac{du_x}{dx} \equiv u'$. The second term is due to the wind force F_{wind}. It varies linearly with the displacements u_x and is scaled by the atomic volume Ω to give an energy density.

In some ways this problem is analogous to that of a solid rod, supported above and below, in a gravitational field: the top of the rod is in tension and the bottom is in compression (Fig. S7). Nature adopts the solution that minimizes the potential energy density $\lambda(u_x, u'; x)$. We find this

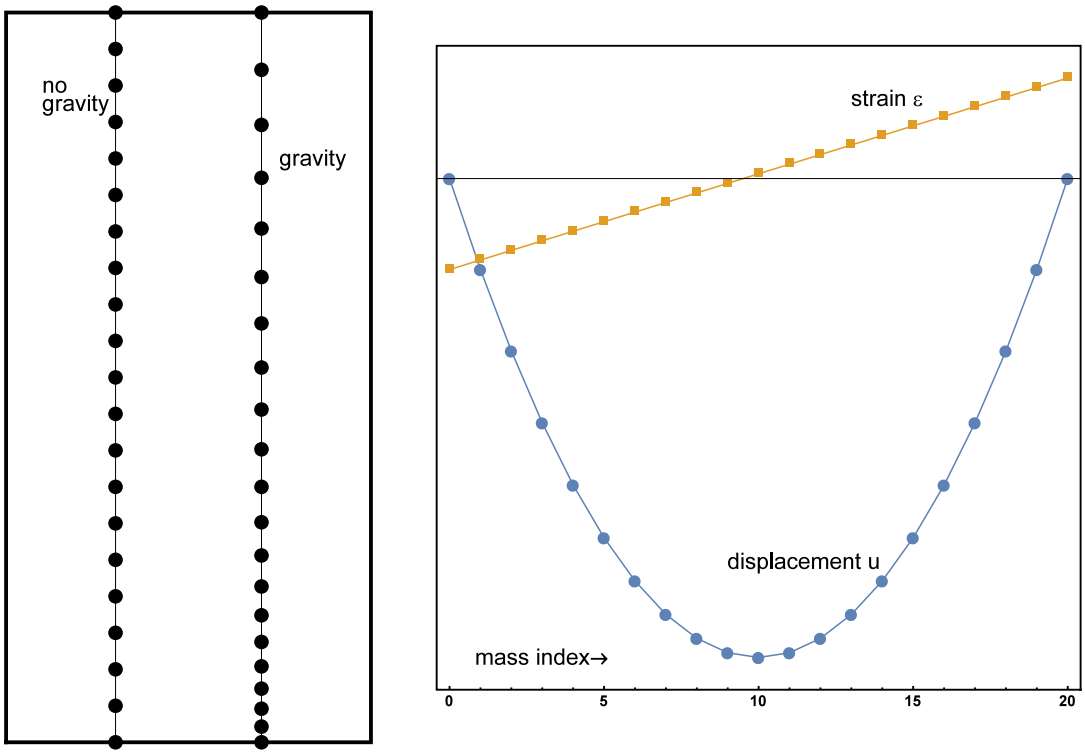

Figure S7: **Vertical rod/mass chain analogy:** A simplified, 1D model considers a vertical rod as a chain of discrete masses m, each connected to its nearest neighbors by springs with spring constant k. Here we show $N = 21$ masses with the 0$^{\text{th}}$ and the 20$^{\text{th}}$ masses both fixed. In the absence of a gravitational field the masses are equally spaced with spacing ℓ. Turning on a gravitational acceleration $g < 0$ puts the top of the chain into tension and the bottom into compression, with the position of the j^{th} mass given by $y_j = j(\ell + \frac{mg}{k}(N+1-j))$. The greatest displacements from the no-gravity positions occur at the center of the chain. This mass-chain model reproduces the functional forms of the strain (linear) and the displacements (parabolic) created by the electron wind force in the center of a current-carrying wire.

However, the analogy of the mass chain in a gravitational field with the current-carrying wire breaks down at the boundaries; the mass chain only gives sensible results if the positions of the end masses are fixed, while in the current-carrying wire the wire ends are free. The analogy works as well as it does because, in the case of a varying cross sectional area A, the wind force decreases $\propto 1/A$. The effective k increases $\propto A$ (for both), with the result that, in the wire's contacts, the combination of a stiffening wire and a vanishing wind force roughly recreates the fixed boundary condition employed for the mass chain. In contrast, because the gravitational force increases $\propto m \propto A$, the strain in the mass-chain grows without bound if its ends are not somewhere fixed.

solution using the calculus of variations. Euler's equation is:

$$\frac{\partial \lambda}{\partial u_x} - \frac{d}{dx}\frac{\partial \lambda}{\partial (u')} = 0. \tag{S12}$$

The wind force is defined as $F_{\text{wind}} \equiv Z^* eE$, where Z^* is the effective ionic charge, $e > 0$ is the magnitude of the electron's charge, and E is the electric field[1]. The product of the wind force F_{wind} and the area A can be written

$$F_{\text{wind}} A = Z^* eEA = Z^* e\rho JA = Z^* e\rho I, \tag{S13}$$

where we have used Ohm's law $E = \rho J$ and the definition of the current density $J \equiv I/A$. In the approximation that ρ is independent of x (i.e. that $\partial\rho/\partial T = 0$), this product $F_{\text{wind}} A$ is a constant independent of position x. Here the gravity analogy breaks down: in the gravity case $F \propto A$, while $F_{\text{wind}} \propto 1/A$. Evaluating Eq. S12 gives

$$-\frac{Z^* e\rho I}{\Omega} = \frac{d}{dx}\left(E_Y A \frac{du_x}{dx}\right), \tag{S14}$$

which can be integrated to give

$$-P = \sigma_x = E_Y \epsilon_x = E_Y \frac{du_x}{dx} = \frac{-Z^* e\rho I}{\Omega}\frac{x}{A(x)} = \frac{-Z^* e\rho}{\Omega} x J(x), \tag{S15}$$

where the x-dependence of the cross-sectional area A is now written explicitly, and where the constant of integration has been set to zero because of the boundary condition $du_x/dx \to 0$ as $x \to \pm\infty$. The stress, or pressure P, in the wire is thus proportional to the electric current I and varies with position like $x/A(x)$. Thus, in the middle of the wire, where A is small and constant, it increases linearly with the distance x measured from the wire center. In the contacts, however, A becomes large so the stress goes to zero.

[1]The net force F on an ion due to the electrical potential applied across the wire may be thought of as the sum of two terms: a 'direct' force due to the electric field E and a 'wind' force created by momentum transfer from the electrical current's charge carriers to the ion[3]. In an Ohmic material these terms are not experimentally separable. Because $Z^* < 0$ in aluminum, the wind force dominates in this material. We therefore refer to the net force as the wind force throughout this paper.

The wire's geometry can be specified by giving its cross-sectional area A as a function of position x along the wire. In the first approximation this function is piecewise continuous (Fig. S8), and can be written

$$\begin{aligned} A_p(x) = & \mathrm{A}_0 \left(\Theta\left[x + L/2\right] - \Theta\left[x - L/2\right]\right) \\ & + \Theta\left[x - L/2\right] \left(\mathrm{A}_0 + m\left(x - L/2\right)\right) \\ & + \Theta\left[-x - L/2\right] \left(\mathrm{A}_0 - m\left(x + L/2\right)\right), \end{aligned} \tag{S16}$$

where $\Theta[x]$ is the Heaviside step function, A_0 is the wire's cross-section, and m is twice the film thickness times the tangent of the opening half-angle of the contacts. To give a more realistic, analytic function for fitting, we convolve $A_p(x)$ with a Gaussian,

$$G(x) = \frac{1}{\sqrt{2\pi}\sigma} \exp\left(-\frac{x^2}{2\sigma^2}\right), \tag{S17}$$

to give

$$\begin{aligned} A(x) = & \mathrm{A}_0 \\ & + \frac{m}{2}\left(x - L/2\right) \mathrm{erfc}\left[\frac{L/2 - x}{\sqrt{2}\sigma}\right] - \frac{m}{2}\left(x + L/2\right) \mathrm{erfc}\left[\frac{L/2 + x}{\sqrt{2}\sigma}\right] \\ & + \frac{m\sigma}{\sqrt{2\pi}} \left(\exp\left[-\frac{\left(L/2 - x\right)^2}{2\sigma^2}\right] + \exp\left[-\frac{\left(L/2 + x\right)^2}{2\sigma^2}\right]\right), \end{aligned} \tag{S18}$$

where the Gaussian width σ (not to be confused with the stress σ) parametrizes the effects of resist shadowing and other resolution limitations of the e-beam lithography.

Both the piecewise continuous function $A_p(x)$ (Eq. S16) and its smoothed counterpart $A(x)$ (Eq. S18) are plotted in Fig. S8. Also shown are the form of the current density $J(x) = I/A(x)$ and the pressure $P(x)$ (Eq. S15), which vary like $1/A$ and x/A, respectively.

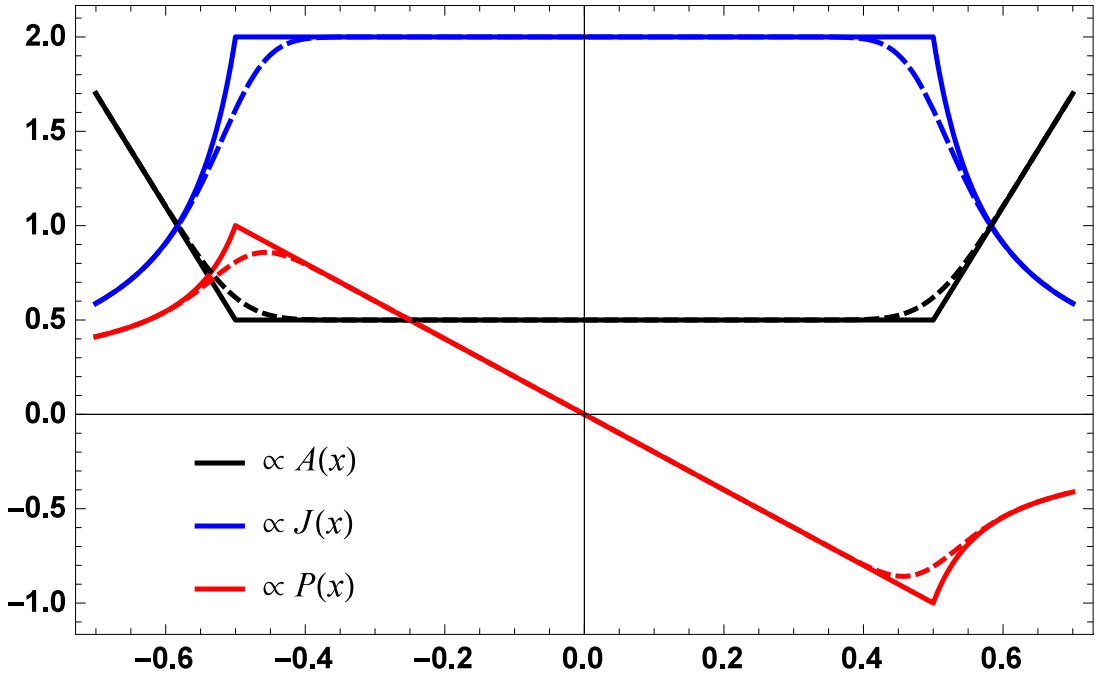

Figure S8: **Functions of the nanowire cross-section for fitting:** With perfect lithography the nanowire's cross section $A_p(x)$, the current density $J(x) \propto 1/A_p$, and the pressure $P(x) \propto x/A_p$ would be piecewise continuous (Eq. S16), as shown here (solid curves) with $A_0 = 0.5$, $L = 1$, and $m = 6$. For display purposes these functions, which have different units, have been normalized such that their amplitudes at $x = L/2$ are 0.5, 2, and 1, respectively. We convolve the piecewise continuous $A_p(x)$ with a normalized Gaussian (here with width $\sigma = 0.05$) to give an analytic $A(x)$ (Eq. S18) and more realistic functions (dashed curves) for fitting.

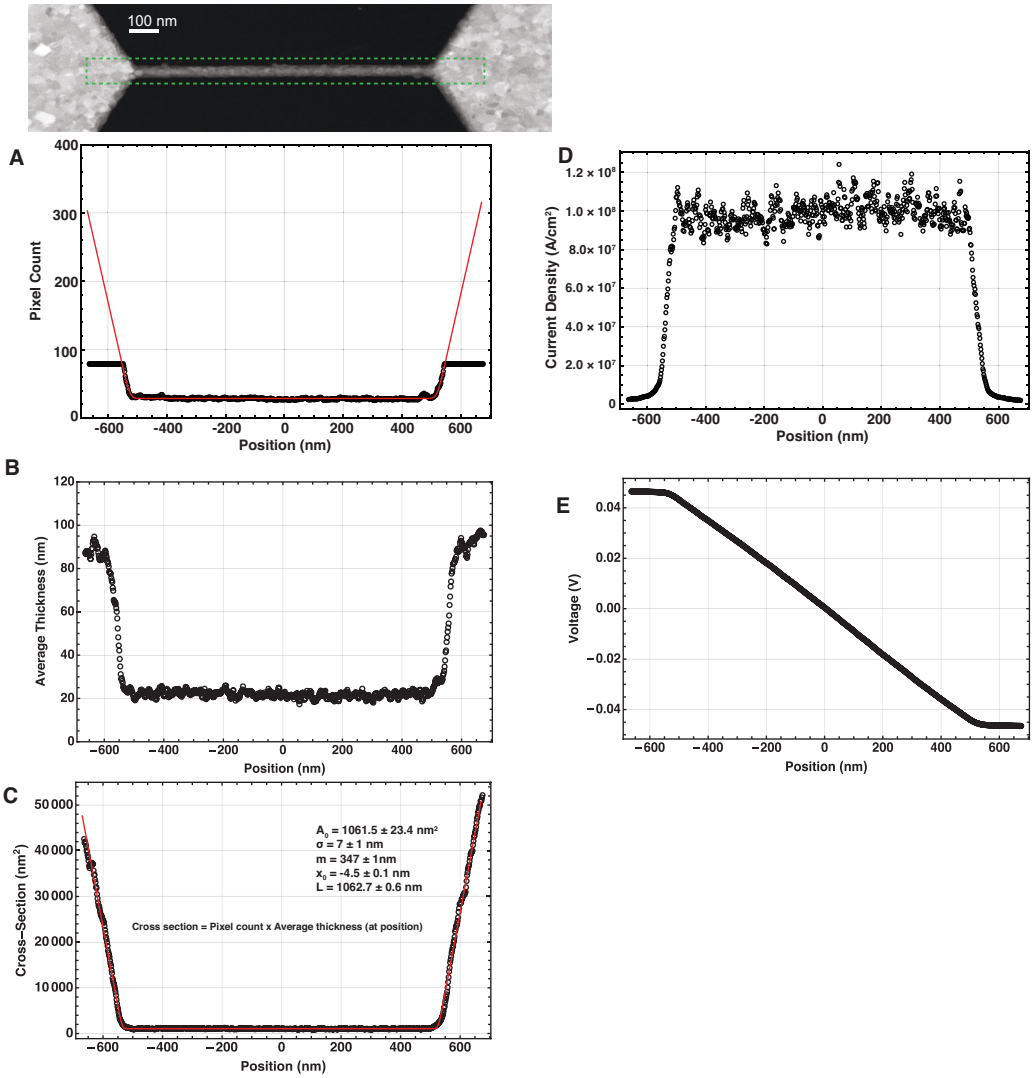

Figure S9: **Analysis of cross-section, current density, and voltage:** The dashed green box in the ADF STEM image outlines the field of view (FOV) of the EELS spectrum image. The number of pixels containing aluminum signal increases linearly as a function of horizontal position between the ends of the wire and the intersection of the aluminum with the vertical bounds of the FOV (**A**, black data). At the latter points saturation occurs: the actual width of the contacts is larger than the value obtained by summing the pixels vertically across the FOV. To account for the saturation we extrapolate the pixel count (**A**, red fit). Multiplying the width of the wire (extrapolated pixel count times pixel size) by the average thickness (**B**, calculated with Eq. S3) gives the cross sectional area (**C**, black data). We fit the nanowire cross section $A(x)$ to Eq. S18 (**C**, red fit), and thereby extract the parameters A_0, L, m, and σ that describe the wire geometry (x_0 describes the wire location relative to the field of view). The current density $J(x)$ (**D**) is computed by dividing the current I (here $+1.03$ mA) by the cross section data $A(x)$ from (C). The electrical potential $V(x)$ along the wire and contacts (**E**) is calculated by numerically integrating the product of the current density (D) with the temperature-dependent resistivity $\rho(T)$ along the wire, using the PEET-determined temperature $T(x)$. In other words, $V(x) = -\int_0^x J(x')\rho(T(x'))dx'$, where $\rho(T)$ is determined from the $I-V$ fit to Eq. S5 (Fig. S6) and $T(x)$ is determined by the fit to Eq. S6 (Fig. 3).

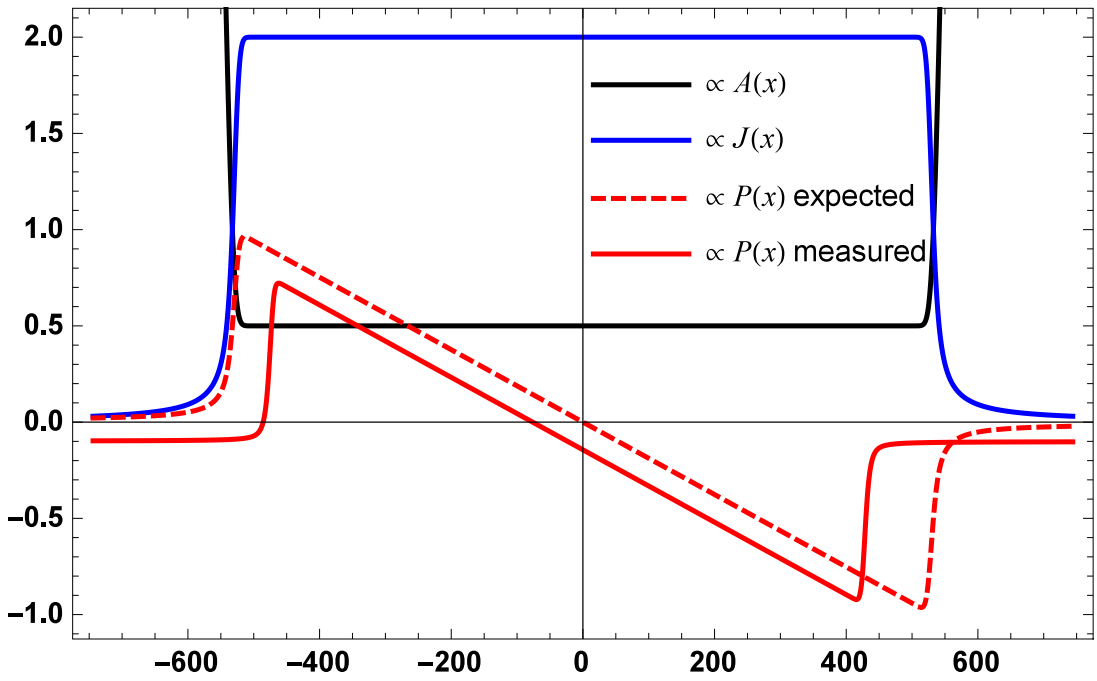

Figure S10: **Functions of $A(x)$ with realistic x-scaling:** The nanowire cross-section $A(x)$ is measured with traditional STEM and STEM EELS (i.e. xy and thickness mapping, respectively), and the current density $J(x)$ scales like $1/A$. According to a classical model (Eqs. S11–S15) of the electron wind force's effect on an elastic wire, the pressure $P(x)$ should scale like xJ. For the nanowire of Figs. 1–3 we measure $L = 1063$ nm, $m = 347$ nm, and $\sigma = 7$ nm with traditional STEM and STEM EELS (Fig. S9). This value for m is within 10% of the value $2 \times \tan(63.2°) \times 90$ nm $= 356$ nm expected based on the measured contact opening half-angle (the angle specified by the e-beam lithography mask is $63.5°$) and deposited film thickness. Plotting the functions $\propto A(x)$, $\propto J(x)$, and $\propto P(x)$, where the overall normalizations are as in Fig. S8, gives the solid curves shown. (The Gaussian smoothing parameter σ is seen to be basically negligible compared to the L and m length scales.) However, fitting the $P(x)$ measured with STEM EELS density mapping returns $L = 920$ nm, $m = 2110$ nm (holding $\sigma = 7$ nm fixed), which gives the dashed red curve (normalized here like the solid red curve). The mechanical model of the wind force's action on the nanowire thus produces a functional form that fits the data well, but that fails to explain the observed spatial dependence of $P(x)$. Specifically, the observed $P(x)$ turns over too soon and reverts to zero too abruptly, returning to its unperturbed value well inside the wire, where the current density is still high.

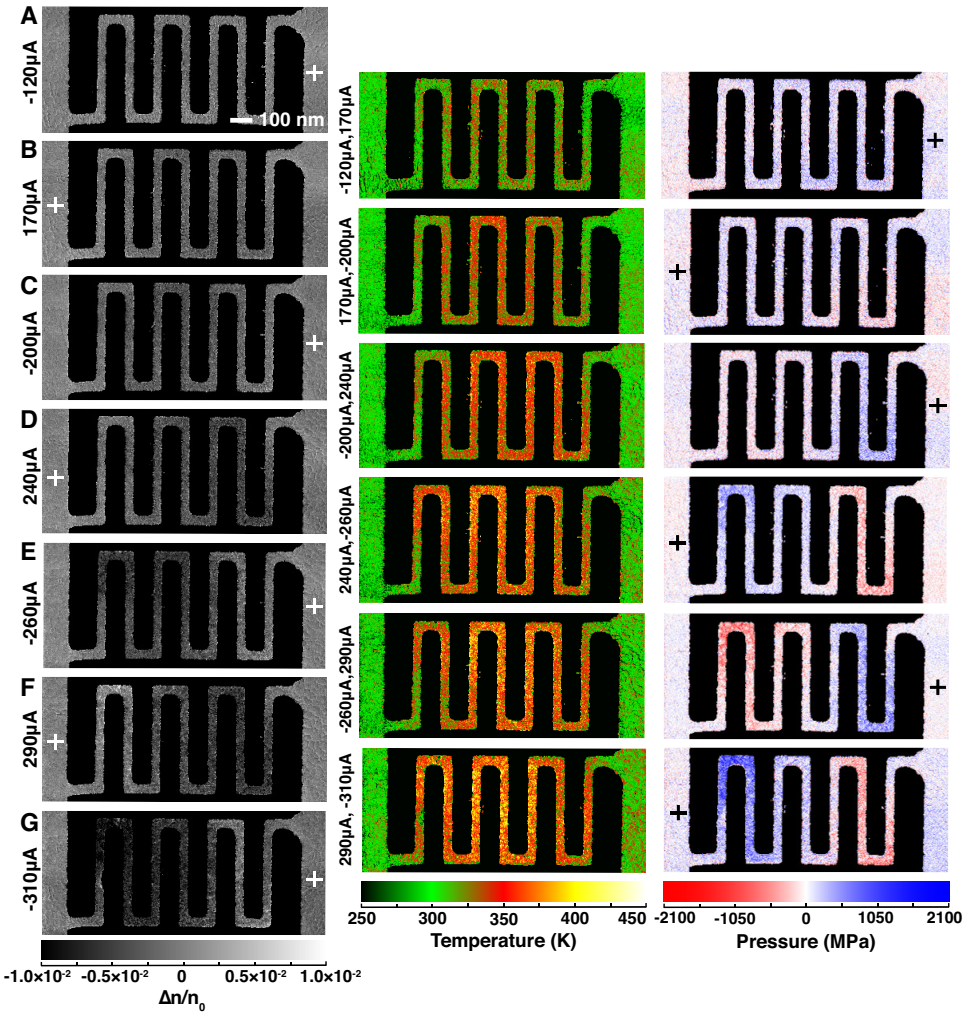

Figure S11: **Similar temperature and pressure profiles occur in serpentine wires:** The left column shows a series of $R \simeq \Delta n/2n_0$ maps, where the applied electrical current is alternating with increasing magnitude from image-to-image from top-to-bottom. (These R maps all are computed using the same initial $I = 0$ reference image.) Plus signs indicate the conventional current source, i.e. the contact the electrons flow toward. To extract approximate values for the current-even (temperature) and current-odd (pressure) effects, we combine maps adjacent in this time series in current-even (center column) and current-odd (right column) combinations, making no correction for the differing current magnitudes. As expected, the current-induced T and P effects both get consistently larger as the current magnitude increases. The T and P effects are also consistently even and odd, respectively, about the wire center, and even and odd, respectively, in the current's polarity. Interestingly, the P effect, like the T effect, is insensitive to curvature in the wire: it is unimpeded by corners. At the largest current value (G), a divot appears on the leftmost of the wire's vertical sections, where the wire is darker and thus in tension. This divot eventually develops into a void and the wire fails. Throughout this data set the P extrema occur well inside the wire, where the current density is still high. Furthermore, the wire fails specifically (frame G, leftmost vertical leg) where the tension is largest, and not where the tension maximum would be expected in a classical wind force model (nor, e.g. where T is large).

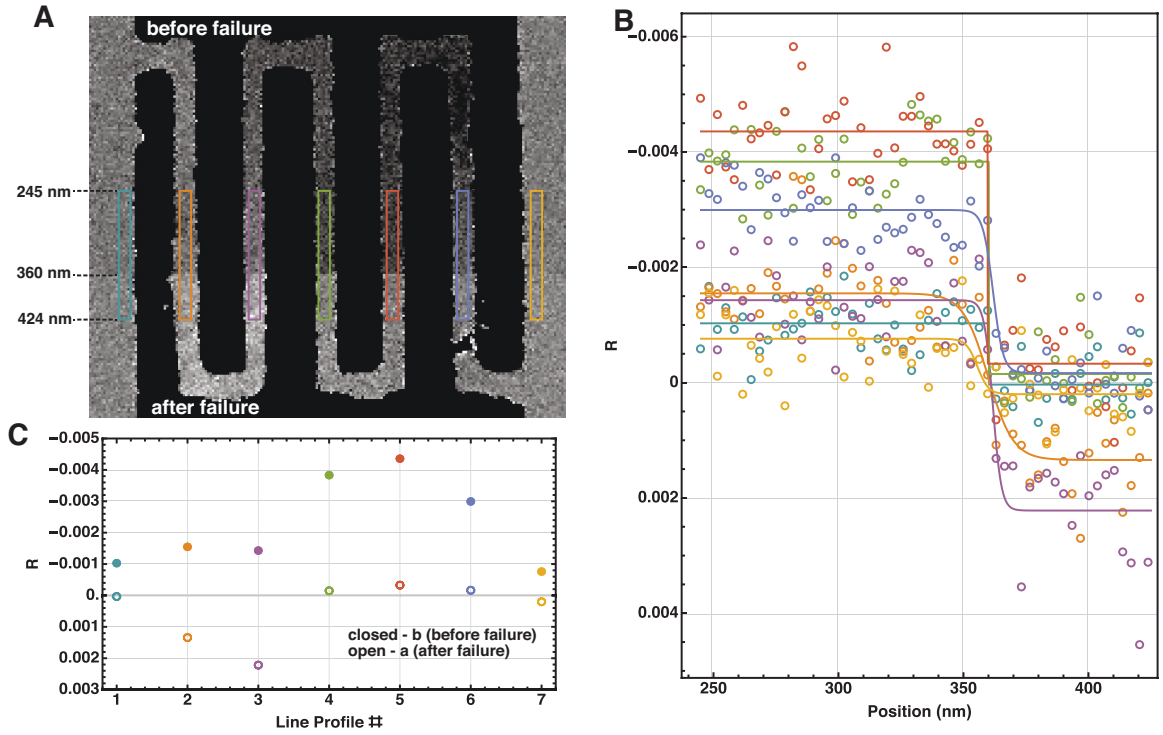

Figure S12: **Speed of elastic response: (A)** This serpentine wire failed near the right contact two-thirds of the way through a spectrum image. The R map shows step discontinuities in every leg, indicating that the wire density returns to its $J = 0$ value within a single row's scan time (198 pixels/row $\times$ 21 ms/pixel $=$ 4.1 s). **(B)** Line profiles extracted by averaging the rectangles in (A) over their narrow directions are fit with hyperbolic tangents. In all cases the transition width is consistent with a step discontinuity. **(C)** The asymptotic values of R 'before' and 'after' (failure) are extracted from the fits and plotted. In the absence of any plastic deformations, the 'after' values would be a line on a horizontal line at $R = 0$. Likewise, the 'before' values would show the simultaneous effects on the density of the temperature and the wind-force pressure — see Figs. 2–3. The spatial distribution of the 'after' asymptotes indicates some plastic deformation, i.e. atomic currents. Subtracting these values from the 'before' asymptotes reveals the prompt effects that depend on the current I. Both the temperature $\propto I^2$ and the pressure $\propto I$ effects show non-zero signatures.

A.2 Fit parameters extracted from spectrum images: maps and line profiles

Figures S13–S17 show maps of the parameters of Eqs. S1–S2 extracted by fitting the spectrum images used to create Figs. 2–3. Below each map is a corresponding line profile that gives the parameter averaged vertically over the non-zero pixels (pixel count plotted in red) only. The 795 pixel $\times 74$ pixel maps displayed are aligned spatially relative to each other and are centered halfway between the points where the pixel count saturates.

Each of Figs. S13–S17 shows one particular perspective on (i.e. slice through) the data. Together they provide concise summary of the entire data set consisting of five spectrum images, each of which is 800 pixels $\times$ 80 pixels $\times$ 2048 energy bins $\times$ 4 bytes/bin $= 0.5$ GB. The main takeaway is that, as a function of applied bias, the variations in μ_{pl} (Fig. S15, right column) are far larger than those of any other fit parameter (Figs. S13–S17). The sensitivity of the center bulk plasmon energy μ_{pl} to density changes, and the relative insensitivity of μ_{pl} to other geometric and chemical factors (e.g. thickness, cladding, support), make it extraordinarily useful for revealing the effects of temperature and pressure.

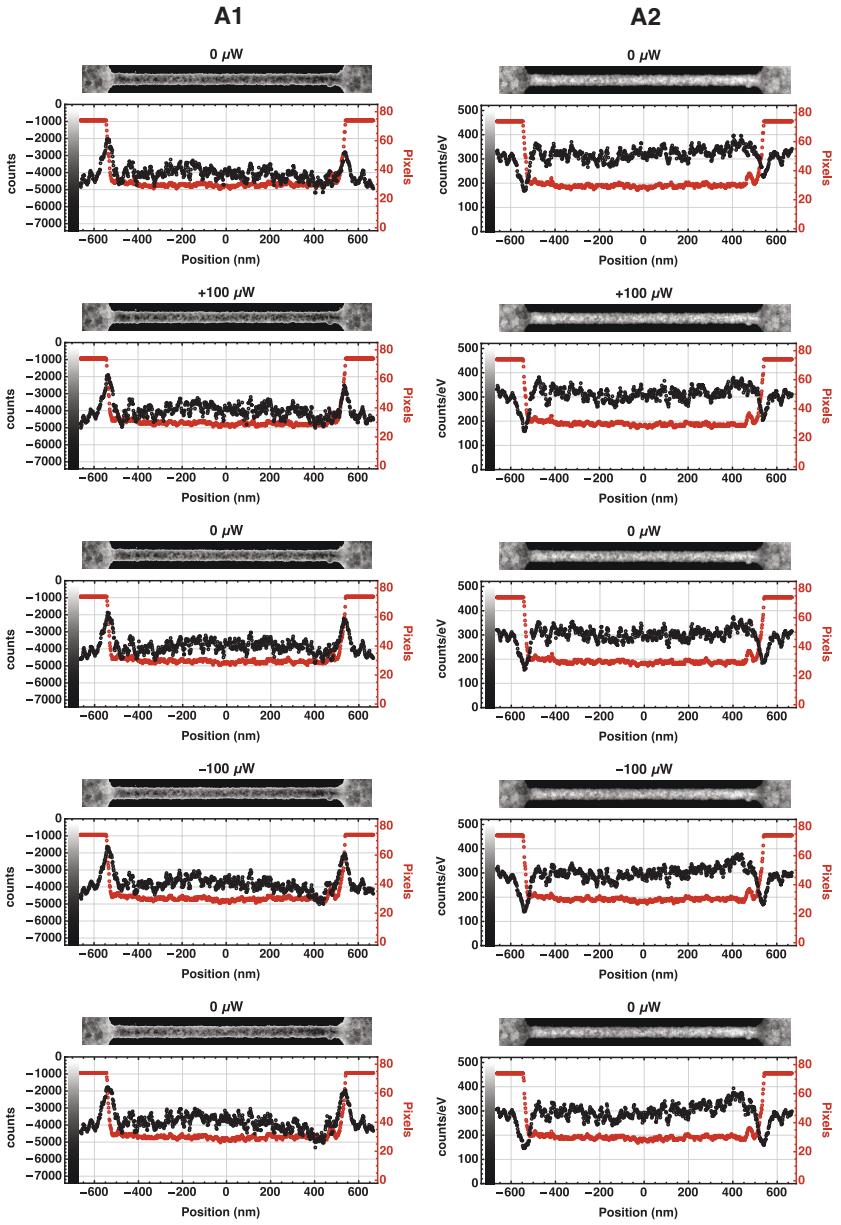

Figure S13: **Slices A_1 and A_2:** Maps and line profiles of the fit parameters A_1 and A_2, which characterize the linear background at the aluminum plasmon (Eq. S2). This background primarily results from the silicon nitride plasmon. The background shows no appreciable variation in the course of the experiment, either as the bias varies or as a function of time.

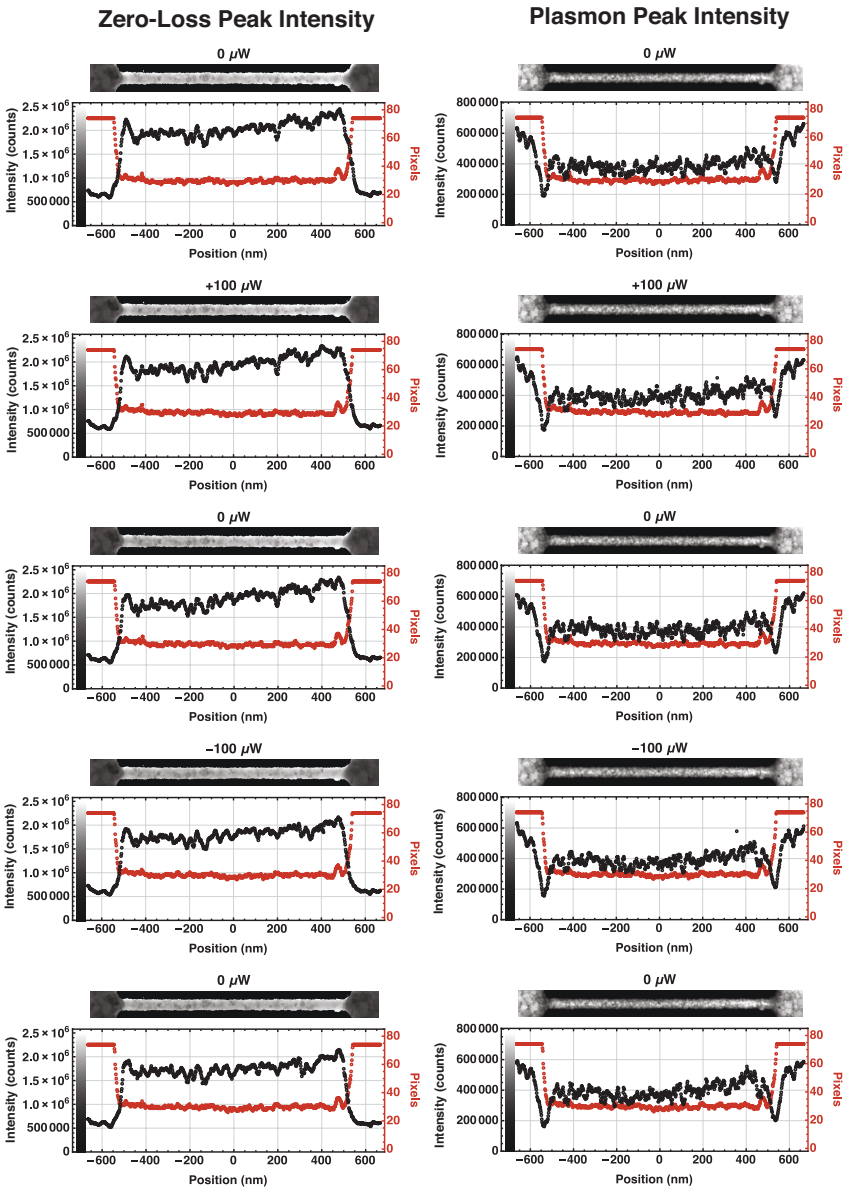

Figure S14: **Slices I_0 and I_1:** Maps and line profiles of the fit parameters I_0 and I_1, which characterize the intensities of the ZLP and the first aluminum plasmon (Eqs. S1–S2). The ZLP intensity is smaller in the contacts, which are thicker than the aluminum wire. Areas with too little aluminum plasmon intensity are not fit. While the ZLP intensity shows no appreciable variation in the course of the experiment, either as the bias varies or as a function of time, the plasmon intensity varies slightly. These variations indicate aluminum thickness changes — see Fig. S18.

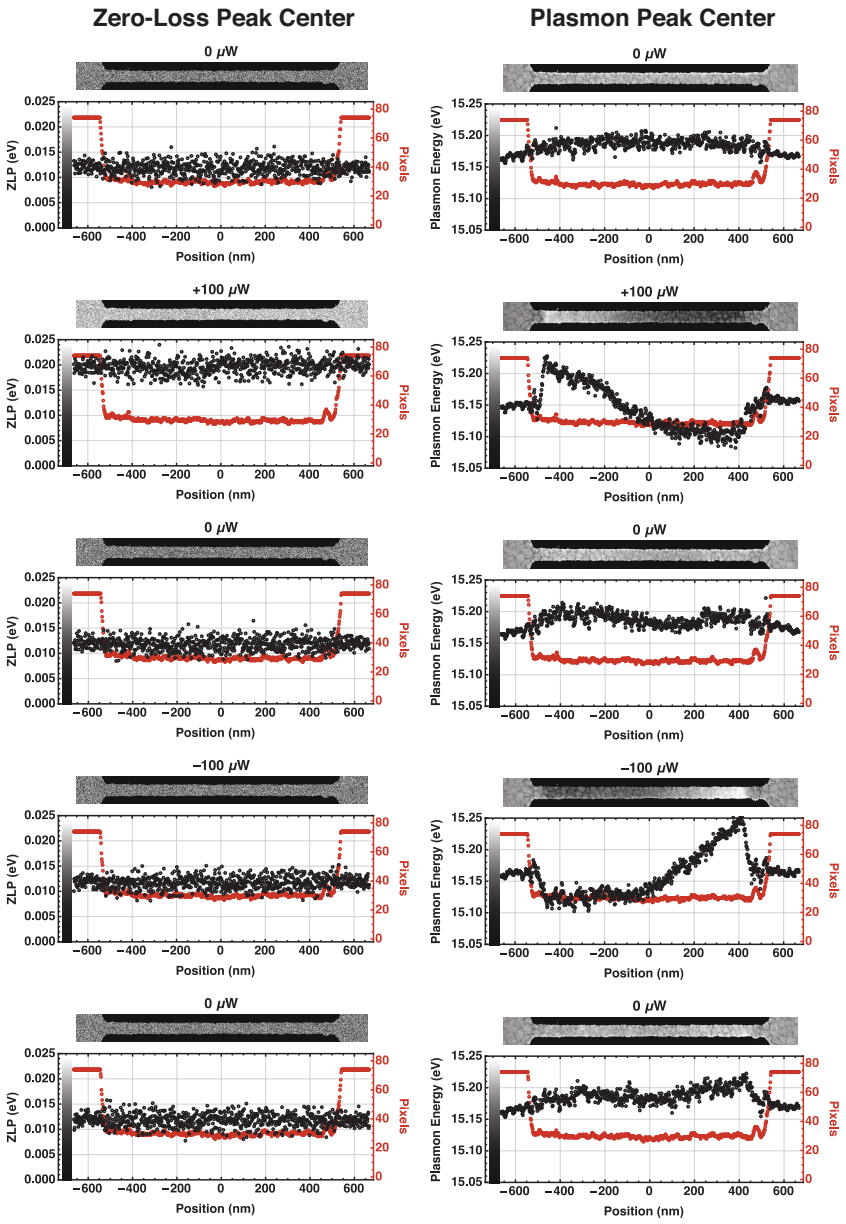

Figure S15: **Slices $\mu_{\mathbf{ZLP}}$ and $\mu_{\mathbf{pl}}$:** Maps and line profiles of the fit parameters μ_{ZLP} and μ_{pl}, which characterize the center energy values of the ZLP and the aluminum plasmon (Eqs. S1–S2). The μ_{ZLP} values define the energy zero. Accordingly the entire spectra have been shifted by an integer number of bins such that the ZLP maximum shown here is within one bin-width of zero. The μ_{ZLP} values have a standard deviation of 0.007 eV, which is smaller than the spectrometer bin width $\Delta_{\mathrm{bin}} = 0.025$ eV. The μ_{pl} data is the same as that shown in Fig. 2. The maps of μ_{pl} show both the grain structure of the aluminum wires (at a grain boundary the values dip by 9–17 meV[22]) and shifts due to temperature and the wind force. Within a grain in the contacts the standard deviation of μ_{pl} is $\sigma_p = 9.8$ meV, which, when compared to the mean $\mu_{\mathrm{pl}} = 15.185$ eV gives a noise-to-signal ratio $\sigma_p/\mu_{\mathrm{pl}} = 0.0006$.

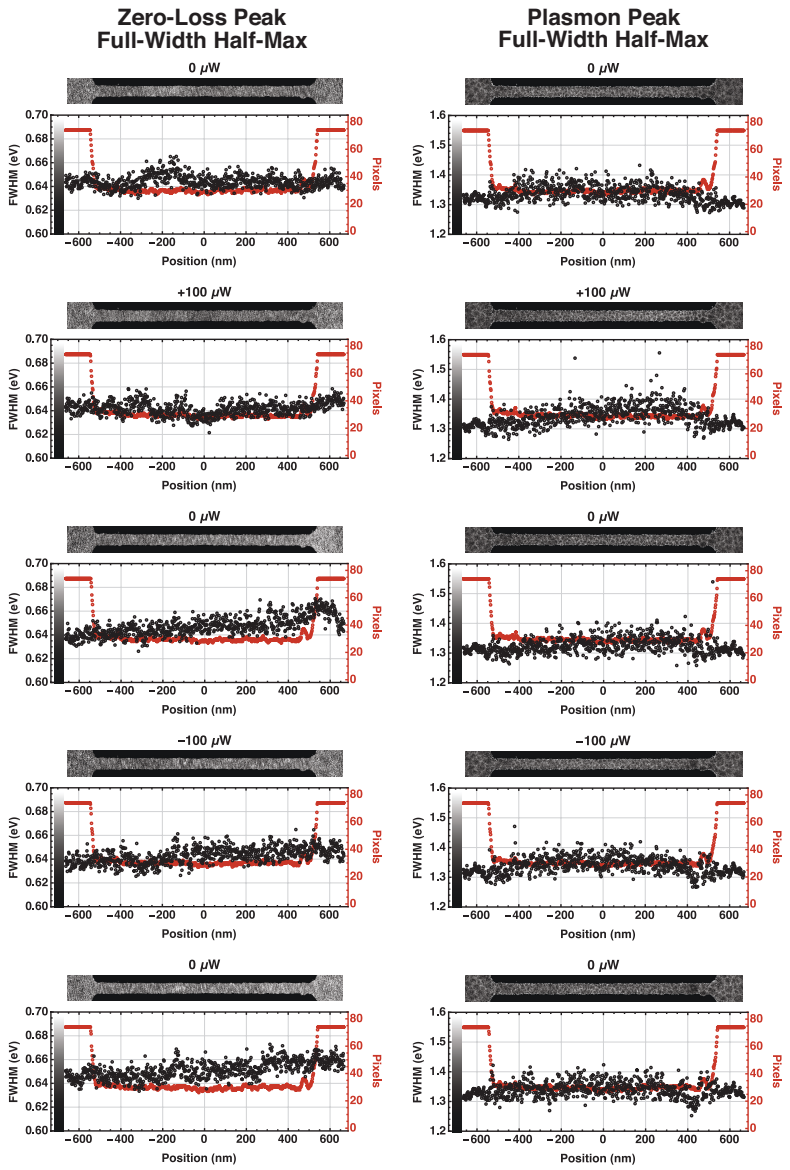

Figure S16: **Slices $\mathbf{FWHM_{ZLP}}$ and $\mathbf{FWHM_{pl}}$:** Maps and line profiles of the fit parameters $\mathrm{FWHM_{ZLP}}$ and $\mathrm{FWHM_{pl}}$, which characterize the full-width at half-maxima of the ZLP and the aluminum plasmon (Eqs. S1–S2). The FWHMs show no appreciable variation in the course of the experiment, either as the bias varies or as a function of time. The ZLP FWHM has an average value of 0.64 eV, and the plasmon FWHM has an average value of 1.3 eV.

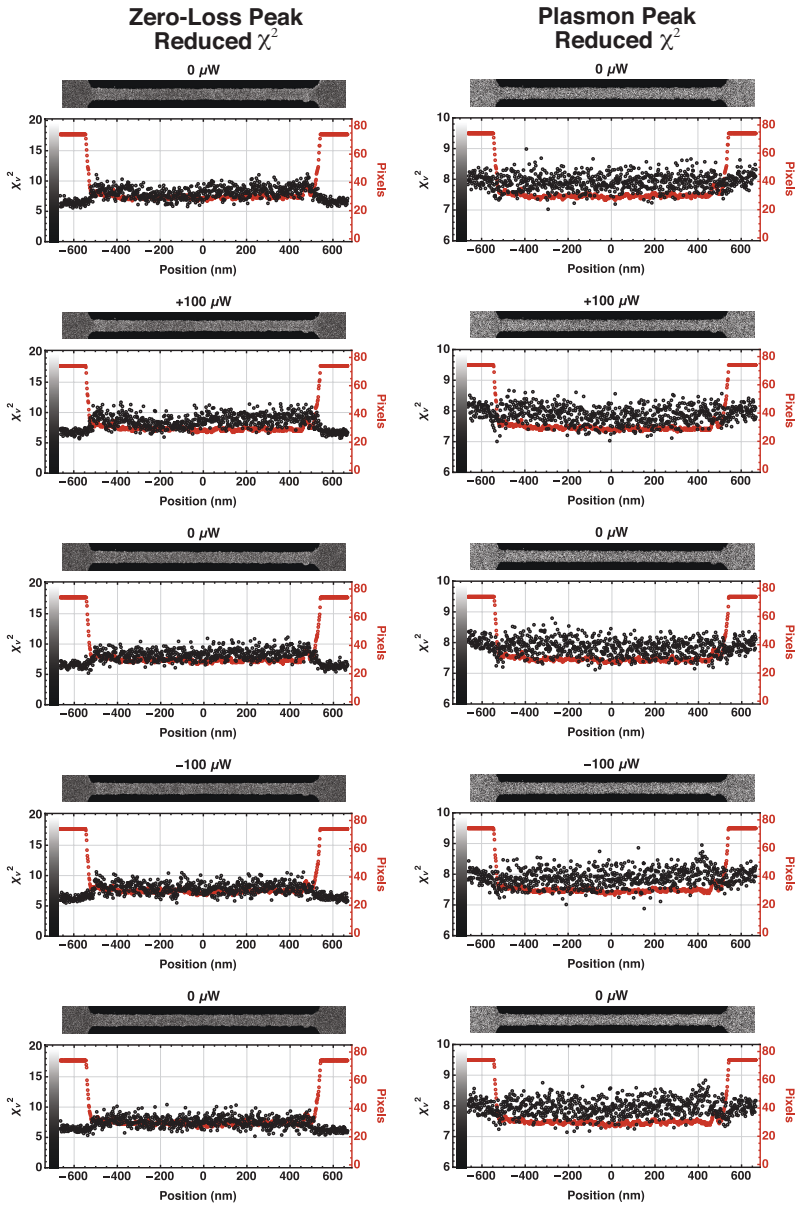

Figure S17: **Slices $\chi^2_{\mathbf{ZLP}}$ and $\chi^2_{\mathbf{pl}}$:** Maps and line profiles of the reduced chi-squared χ^2 values for the Gaussian (Eq. S1) and Lorentzian fits (S2), which show the goodness of the fit. In each case the fit windows (± 0.2 eV for the ZLP, and 13.75–16.6 eV for the plasmon) are chosen to minimize the χ^2 parameter.

A.3 Atomic currents

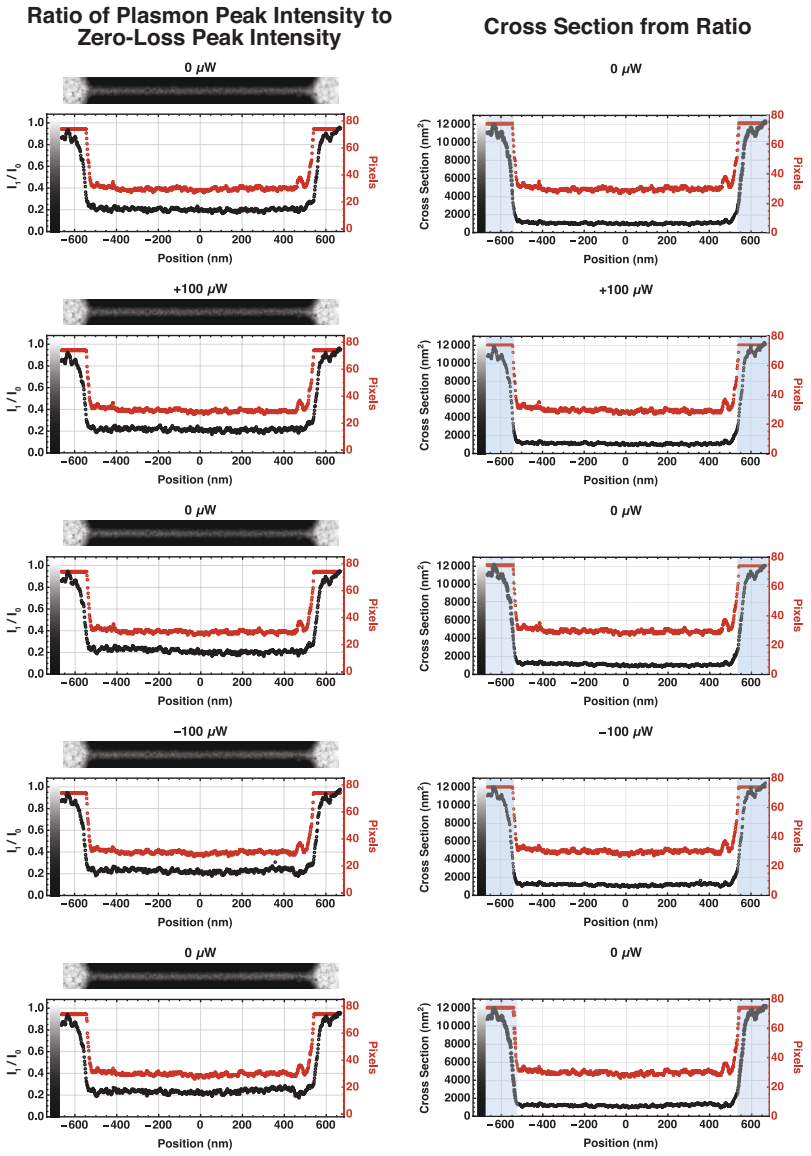

Figure S18: **Thickness from I_1/I_0 ratio:** Maps and line profiles (left) of the ratio I_1/I_0 give an estimate of $t_{\mathrm{Al}}/\lambda_{\mathrm{Al}}$ (see discussion after Eq. S2). These data show the contacts to be thicker than the center of the wire. The corresponding cross section profiles (right) are calculated by applying Eq. S3 to the maps on the left, summing across the maps' vertical dimension, and multiplying by the pixel size. The cross section profiles have not been corrected to account for the extent of the contacts outside the field of view (see Figs. 1, S9), so in the right-hand column the cross section values in the blue bands (where the pixels value is constant) are smaller than the actual cross section.

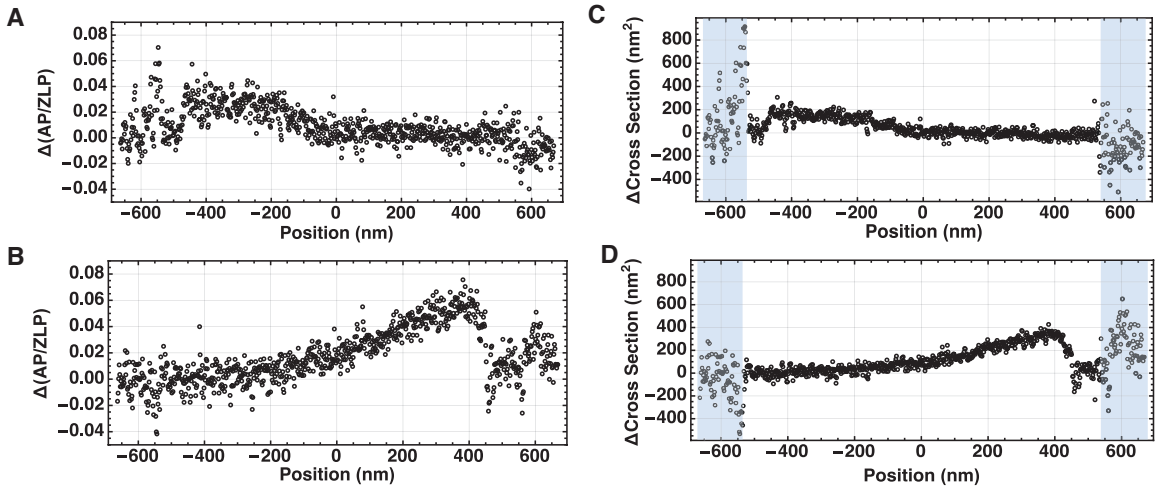

Figure S19: **Atomic currents: thickness.** The thickness profiles of Fig. S18 are almost indistinguishable. However, subtracting the 1st from the 3rd (**A**) and the 3rd from the 5th (**B**) reveals some systematic differences. Running the (conventional) electrical current from left-to-right cause the thickness to increase on the left side of the wire (A). Reversing the current causes the thickness to increase on the right side of the wire (B). These thickness changes have corresponding effects on the wire cross section (**C** and **D**, also derived by subtracting panels from Fig. S18). As explained in Fig. S18, the values in (C) and (D) in the blue bands are not reliable.

The changes in cross section in (C) and especially (D), which represent plastic deformations, have a similar spatial profile to that of the pressure (Fig. 3), which reflects the elastic wind force. In particular, the changes in both the thickness and the cross section peak well before the wire widens into the contacts.

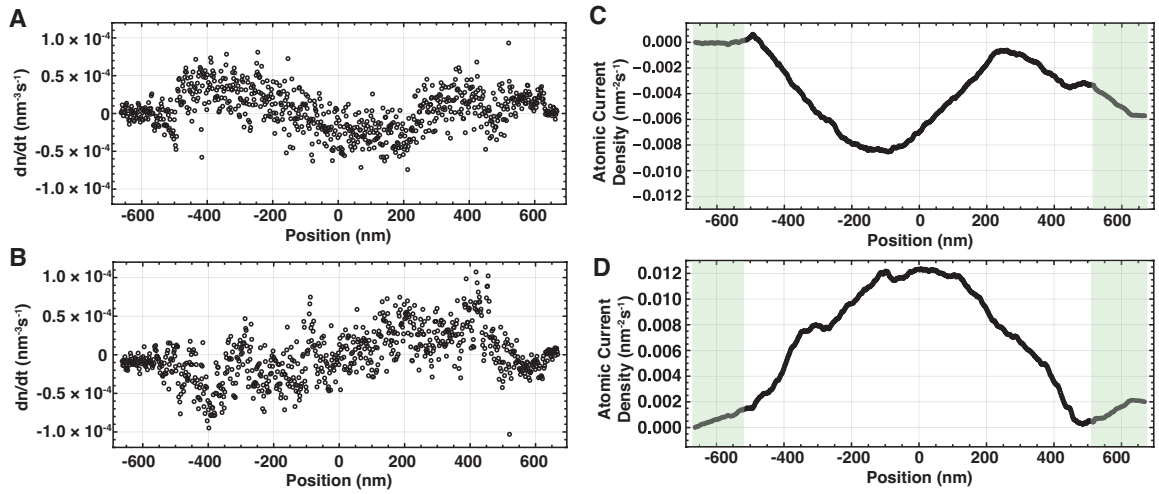

Figure S20: **Atomic currents: density.** Systematic differences in the plasmon energy maps with zero electrical current (the 1st, 3rd, and 5th scans of Fig. 2, shown again in the right-hand column of Fig. S15) indicate that the electrical current applied during the 2nd and 4th scans moves some atoms. To quantify this atomic current J_a, we invert Eq. 1 to find the electronic number density $n = (E_p/\hbar)^2(\epsilon_0 m/e^2)$ in terms of the plasmon energy E_p. Applying this relation to the Fig. 2 zero-current E_p line profiles and subtracting, we find, after dividing by 3 (the ratio of the electronic number density n to the atomic number density n_a) and the scan time (42 minutes), the time rate of change of the atomic number density dn_a/dt during the 2nd (**A**) and 4th (**B**) scans. Using the 1D continuity equation $\partial n_a/\partial t = -\partial J_{ax}/\partial x$, we then numerically integrate the curves **A** and **B**, starting at the left boundary, to find J_a along the wire axis (x) during the 2nd (**C**) and 4th (**D**) scans. Green bands in (C) and (D) indicate regions where the J_a values are not reliable because the 1D approximation is not good in the contacts.

In a zeroth-order approximation we would expect J_a to have a 'top-hat' profile like that of the current density, i.e. $J_a \propto J$. However, the atomic diffusion constant is exponential in the temperature, and the wire is hottest at its center. Accounting for the spatial variation of the diffusion constant gives a roughly parabolic J_a profile, as seen in **D** and, to a lesser extent, **C**. Both **C** and **D** show the four main qualitative features that we expect, namely that J_a (i) is in the same direction as J, (ii) changes sign with J, (iii) has its largest magnitude near the wire center, and (iv) goes to zero at the contacts.

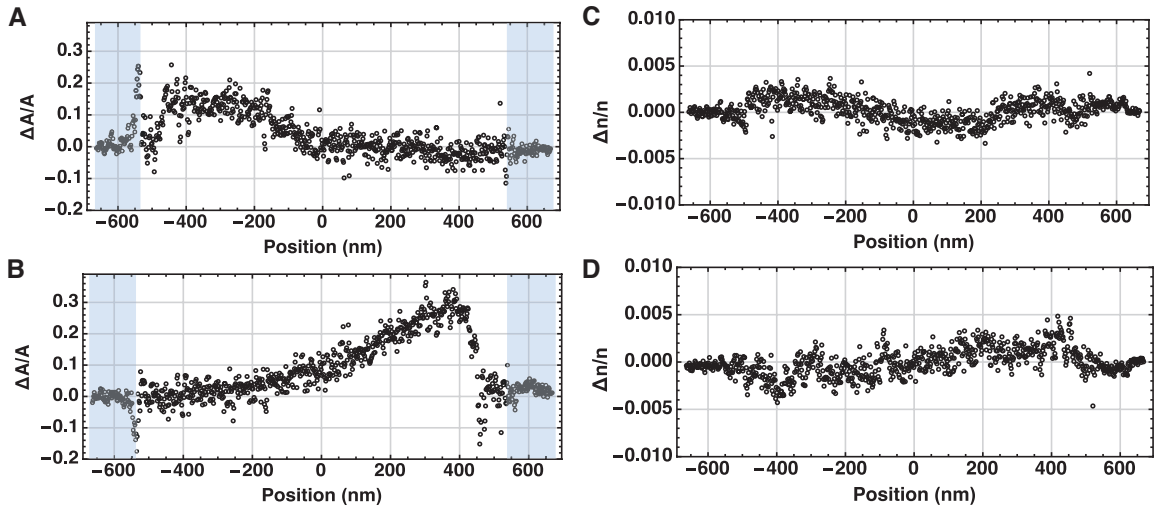

Figure S21: **Atomic currents: thickness-density comparison.** We consider the atomic current as consisting of two components: an cross-sectional area-changing component (Fig. S19) and a density-changing component (Fig. S20). To compare the magnitudes of these two components, we write the total number of atoms N_a in terms of their number density n_a with $N_a = n_a V$, which can be differentiated to give $\Delta N_a/N_a = \Delta n_a/n_a + \Delta V/V \simeq \Delta n_a/n_a + \Delta A/A$. Normalizing the changes in the cross section (Figs. S19 C and D) by its mean value gives $\Delta A/A$ (**A** and **B**, respectively). Similarly, normalizing the changes in the density (proportional to Fig. S20 A and B) by its mean value gives $\Delta n_a/n_a$ (**C** and **D**, respectively). Comparing A and B above with C and D, we see that the area-changing atomic current is roughly $\times 100$ larger than the density-changing current.

Because the experiments are so brief, these atomic currents (which result in plastic deformations) produce negligible stress in comparison to that of the prompt (i.e. elastic) response to the wind force (Figs. 2 and S15).